PNC TN9410 97-059

公開資料

Stirring-induced vortical motion measured by ultrasound Doppler velocimetry: Initial 2D vector plots.

April 1997

Oarai Engineering Center
Power Reactor and Nuclear Fuel Development Corporation

複製又はこの資料の入手については、下記にお問い合わせ下さい。
〒311-13　茨城県東茨城郡大洗町成田町4002
動力炉・核燃料開発事業団
大洗工学センター
システム開発推進部・技術管理室
I nquiries about copyright and reproduction should be addressed to: Technology Management Section, O-arai Engineering Center, Power Reactor and Nuclear Fuel Development Corporation 4002 Nareta-machi, O-arai-machi, Higashi-Ibaraki, Ibaraki-ken 311-13, Japan.

動力炉・核燃料開発事業団（Power Reactor and Nuclwar Fuel Development Corporation）1996

COMMERCIAL PROPRIETARY
PNC TN9410 97-059
June, 1997

Stirring-indueced vortical motion measured by ultrasound Doppler velocimetry: Initial 2D vector plots.

A. Tokuhiro[1] and J. Kobayashi[2]

Abstract

An experimental investigation on stirring-induced vortical motion of a liquid was conducted in a cylindrical container measuring 280mm diameter x 280mm height. The test medium was water and a magnetic stirrer located at the bottom on the container (centered) induced the flow. The motion can be generally described as rotationally induced vortex motion, which is of relevance to gas entrainment concerns from the free surface of pool-type LMFBR.

The objective of the investigation were two-fold: 1) to demonstrate that a two dimensional (2D) velocity field, using ultrasound Doppler velocimetry and a multiple number of ultrasound transducers (TDXs), could be measured and 2) to evaluate the content of the measured velocity information with respect to understanding the relevant vortex dynamics.

Our results show that our first objective was fulfilled; that is, using 6 orthogonally situated TDXs to measure the V_r and V_z components of the flow field, a 2D vector field plot of a segment of the meridional plane was generated and shown to change with the rate of induced flow (rotation rate). However, because the number of TDXs used (6) were small, the coarse resolution of the velocity field limits the amount of velocity information. Therefore traditional data presentation methods to evaluate average and fluctuating quantities under steady and stepwise viewed transient conditions, are indispensible for data analysis. The measurement method holds promise as a useful tool in thermohydraulics as the number of TDXs is increased and therefore the spatial resolution. Some of these possibilities are described in this report.

---

[1] Reactor Engineering Section, Safety Engineering Division, PNC International Fellow.
[2] Reactor Engineering Section, Safety Engineering Division.

公　開　資　料
PNC TN9410 97-059
１　９　９　７年６月

撹拌子による強制渦の超音波ドップラー流速計による計測
予備試験での２次元速度分布

A. Tokuhiro[1]、小林　順[2]

要旨

プール型の高速炉は自由表面を有する構成となっており、自由表面からのガス巻き込みの炉心に与える影響を明らかにすることが重要な研究課題の１つとなっている。原子炉工学室では、ガス巻き込みに対する基本的な知見を得るため、円筒容器内に強制渦を作り出し、強制渦の流動に関する試験を実施している。一方、当室では、音響手法による流速分布計測手法の高度化研究として、超音波流速分布測定装置を用いた多次元計測や液体金属の流速分布測定についても研究を進めている。

そこで渦の流動挙動に関する理解を得るため、ガス巻き込み試験装置に超音波流速分布測定装置を用いた多次元計測手法を適用する実験を行った。

本報告書では、計測された流速情報を評価することにより得られた、渦に対する知見を報告するとともに、超音波流速分布測定装置と多数本の超音波トランスデューサを用いることにより、２次元の流速場が計測できることを示す。

実験は、水を用い、直径280mm×高さ280mmの円筒容器の底面中央におかれた磁石の撹拌子によって強制渦を誘発し、６本のトランスデューサを直交させて設置することによって流速の径および軸方向成分を計測した。

実験の結果、得られた流速データを組み合わせることにより、r-z平面の２次元の流速ベクトル場が得られた。そして、強制渦の流れの変化の比率（すなわち渦度）が示された。

本報告書の結果では使用したトランスデューサの本数が少ないため、流速場の解像度が低くなり、流速情報が限定されたものになっている。したがって、平均値や定常または規則的な過渡変化状態における変動量を評価するためには、レーザー流速計や従来から利用されている可視化技術などを並行して利用する必要がある。しかしながら、超音波流速計を用いた計測方法でも、トランスデューサの本数を増加し、平面解像度を高くすれば熱流動研究上有効な道具となりうることを示した。今後さらに３次元計測に対しても拡張を行っていく。

---

[1] 大洗工学センター　安全工学部　原子炉工学室　国際特別研究員

[2] 大洗工学センター　安全工学部　原子炉工学室

Contents

List of Figures

List of Figures in Appendices

1. Introduction

The unforeseen entrainment of gas bubbles into the coolant loop, especially into the channels cooling the fuel rod assemblies has been a topic of concern in thermohydraulics for both single-phase water and liquid metal cooled nuclear reactors One early investigation was by Winterton [1]. When a void of unknown size enters the coolant channel it may or may not initiate a transient of thermal, nucleonic or combined origins. Thus for the safe, reliable and predictable operation of a LMFBR, the inception of gas entrainment must be monitored from an operational standpoint and/or prevented from a design aspect.

One obvious source of gas entrainment is from the free surface of a pool-type reactor. Here due the flow of coolant just beneath the free surface, gas may be ingested through on of the following mechanisms: 1) through entrapment of gas voids by breaking waves, 2) entrapment of gas through a impact of waves at a solid boundary, 3) ingestion of gas from jetting-type flows penetrating beyond the free surface from below and 4) in the wake region of structures, where rotational flows are likely to be originated. In the latter, if the oncoming flow has enough momentum, conditions may be reached wherein a swirling vortex may entrain nearby gas bubbles or the tip of the (gas core) vortex itself may tear off to yield a gas void. While the impaction of waves at solid boundaries and breaking of surface waves are related phenomena, wave-, jet- and rotation-induced flows are each inherently different dynamically and are receiving attention in LMFBR thermohydraulics.

Prior to developments in the LMFBR fields, gas entrainment into pumps was of concern to hydrologists. Here, in the field of hydraulics (water flows) where pumps are an indispensible component, any incidence of gas ingestion into the pump, from a line upsteam, prevents the steady and reliable operation of the pump. In fact pump failure can occur as a result of repeated gas ingestion induced vibrations. Therefore, the origin of vortices and the prevention thereof, by either active and passive means, has been a point of interest in the hydraulics field. It then follows that some description of phenomena of relevance to the subject at hand and design guidelines are contained in standard handbooks on hydraulics and pumping applications [2].

Though the relevance of gas entrainment in free surface dynamics of LMFBRs has not changed, the level of research activity in the area has declined in the past 20-25 years. Surface wave phenomena on the other hand has received a fair bit of attention in the past 10 years with the advent of more powerful computers to run large numerical simulations. It is now possible to simulate some aspects for example of wave breaking [3] and sloshing in a tank [4]. In the experimental field, computer technology has also made it possible to realize two particular measurement methods useful to the quantification of these types of flows (and others): 1) Ultrasound Doppler Velocimetry (UDV) and 2) Particle Image Velocimetry (PIV). Unfortunately however, both techniques have yet to be widely applied to vortical and other free surface flows. A few investigations such as those by Dolias [5] and Okamoto [6] have investigated vortical flows originating from respectively, flows coming from opposite directions in a rectangular channel (drain-type) using a auto-correlation PIV (photographic) technique and that induced by tangential flow into a tank with a drain at the bottom . Our present application of the UDV technique may thus be one of the first in vortical flows.

In this respect, the objectives of this present investigation are simple and two-fold as follows: 1) to demonstrate that a two-dimensional (2D) velocity field, using ultrasound Doppler velocimetry and a multiple number of ultrasound transducers (TDXs), can be realized and the field of interest measured and 2) to evaluate the content of the measured velocity information with respect to understanding the relevant vortex dynamics.

2. Experiment

2.1 Experimental set-up

Figure 1(a) depicts a schematic of the experiment while **Fig. 1(b)** shows an image of the actual set-up as digitized from video. The experiment consists of an acrylic, cylindrical tank, 290 mm in outer diameter (280 mm inner) and 300 mm height, with a wall thickness of 5 mm. While the tank could simply be was placed on top of a magnetic stirrer (platform) for experiments to begin, since we wanted to study a physically symmetric flow, we centered the tank with respect to the platform. For velocity measurements, up to six 4 MHz ultrasound transducers (TDXs) with an active diameter of 6 mm [casing diameter = 8 mm] were affixed to the side-wall of the tank or lowered to just above the free-surface as shown. The transducers at the side-wall measured the radial component of velocity, V_r, while the "top" TDX measures the axial component of velocity, V_z. De-mineralized water was our test medium while Expancel X-90 powder was used as our ultrasound reflectant tracer. The Expancel X-90 has a specific density of 1.02 and has a nominal, spherical size of 50 μm. As for the concentration of tracing powder, typically 0.8 grams of powder diluted in ~17.24 liters of water (water level 280 mm).

Two types of magnetic stirrers and stirring bars were used in the experiment. The first series of data were taken with the Barnstead/Thermolyne Cimarec 3 magnetic stirrer, which had a operational range of 260-440 rpm, while the Iuchi HPS-500R stirrer had a wider range from 110-1450 rpm. With both stirrers a Ono Sokki HT4100 handheld optical (IR) tachometer was used to measure the rotation rate of the motor. There was however a discrepancy between the tachometer and the "rpm" display attached to the Iuchi stirrer. In this case, a calibration curve plotting the "rpm" display versus the tachometer reading (under conditions of the experiment) was generated for the rpm of interest.

The 6 TDXs were connected to a JcAir 53/63/64 Multiplexer (MPX) unit designed for the time being to work with up to 20 ultrasound TDXs [7]. The unit is card-based so that it is capable of eventually handling 60 TDXs. The unit functions as a multiplexer with a software-driven parameters menu; that is, it is an electro-mechanical switching device that switches off-and-on from one channel (connected to a TDX) to the next with adjustable timing. The software program which runs on an IBM-compatible, DOS-formatted PC enables the user to change five parameters, these being: 1) the trigger time, 2) the hold time, 3) the wait time, 4) the number of cyles and 5) the wait between cycles. Since these parameters can be changed independently of the velocity data acquistion program (in the UVP X-3), the user has to confirm that the time required to accumulate a total of 1024 profiles is nearly the same as that taken by the multiplexer over its specified number cycles and channels. Otherwise either the MPX will cycle through each TDX before 1024 profiles are taken or 1024 profiles will be recorded before the MPX cycles through each TDX. Under some circumstances one or the other "mismatch" may be desireable. These MPX parameters are schematically described in Appendix B, Figure B-1. In the present experiment we found the following settings to be appropriate: trigger time = 20 msec, hold time = 300 msec, wait time =18000msec(18 sec), cycles=6 and wait between cycles = 100 msec. The UVP was set-up to take 170 profiles/TDX for 6 TDXs (6 x 170 = 1020) so that 4 profiles were left empty or contained "noise".

Velocity measurements were taken using the Met-Flow Model X-3 Ultrasound Velocity Profile (UVP) monitor with either a Delrin-encased (temperature limit ~ 80°C) or stainless steel encased Imasonic transducer, both operating at 4 MHz [8]. The transducer had an active crystal diameter of 6 mm. The UVP works on the principle of ultrasound Doppler echography; that is, the position and velocity information are evaluated respectively from the detected time-of-flight and the Doppler-shift frequency at each of 128 locations along the ultrasound beam. Thus, a componental velocity profile is constructed along the measurement line (ML) of the ultrasonic beam. By componental it is understood that the velocity vector oriented either toward or away from the face of the transducer (from the sign of the Doppler shift) while the magnitude is measured at each of the 128 "coin-like" volumetric elements during each of the 1024 measurement intervals. The real-time corresponding to 1024 measurement intervals is adjustable depending largely upon the preference (and experience) of the user, though it should be based on the phenomenon of interest in the flow; that is, based on estimates of the time-scales associated with various transport phenomena, the user is able to select either a short or long time span between measurements. The UVP can also detect transient phenomena. As for calibration of the device, because the UVP is PC-based and thus to its (PC) internal clock, it does not need calibrating in the traditional sense. There is however, a standard device consisting of solid-body rotation of water in a cylindrical container, the resulting (measured) velocity distribution of which can be compared to a known analytical solution. These and related developments and applications of ultrasound Doppler method in thermohydraulics are contained in Takeda [9, 10, 11, 12].

The ultrasound is reflected from tracer particles, typically a plastic based powder with a nominal size of 50-100 μm, that are added to the test medium (water). One should note that the inherent assumptions in using this measurement technique are that: 1) the tracer particles accurately reflect the velocity profile of the liquid state and 2) the modification of the flow field due to addition of tracer particles; that is, the particle-to-fluid interaction, is of minor consequence to the measured profile. Additionally, it is assumed that particle-to-particle interactions are negligible since the concentration of tracer particles, i.e. on the order of 0.046 grams per liter of water, is physically very low. Finally, in the first assumption, the statement "accurately reflects the velocity profile of the liquid state" means *ideally* that there is no slip (relative) velocity between tracer particle and liquid; that is, the particle moves exactly as a fluid element would, as dictated by the initial and boundary conditions of the flow. In reality, this is likely not so, in which case the assumption is that the slip velocity is of negligible consequence and the error associated with the velocity measurement is within an acceptable range. Though the UVP operating parameters were varied, the most common setting was as noted in Appendix A, Fig. A-1. The typical measurement time was of the order of 1-3 minutes.

2.2 Experimental parameters

The typical experimental parameters in terms of the UVP X-3 and MPX are given in Appendices A and B. In order to check the validity of measurement, UVP data at a given roation rate was taken twice, once during the "up" sequence and a second time during the "down" sequence. The "up" and "down" simply refer to the sequence defined by incrementally increasing or decreasing the rotation rate resepctively. In this manner we also checked for any hysterises effects in the flow phenomena.

3. Results and Discussions

3.1 Image data

Figures 2 and **3** show a sequence of images as digitized from video recordings. The negative of the actual video image is shown since the contrast here depicts the vortex more clearly. In the former figure the vortex is shown along with the free surface and an approximate scale for 4 representative rotation rates. One can clearly see that as the rotation rate increases the depth of the vortex with respect to the free surface increases as well. In addition in contrast to lower rotation rates the tip of the vortex appears more pointed at higher revolutions. In the latter figure we show a sequence of images taken one frame at a time. One sees that although there are differences in the shape of the vortex at constant "rpm", the differences are small so that not much information can be drawn from these images. Nevertheless we include these to orient the reader.

3.2 UVP velocity data

3.2.1 1D velocity profiles

We begin with conventional velocity profiles of the V_r and V_z components of the velocity field in the upper region of the container, defined above by the free surface and vertically by the container's wall. We first show in **Figure 4** the average V_r-velocity and its standard deviation distributions. One can see that as expected the central region has the largest velocities, due to the centrifugal (rotational and inertial) forces. The profile is roughly symmetric about the maximum value as it should be. As for the SD-distribution, the left hand portion is similar to the velocity, but diminished while the right region shows a larger scatter of points in contrast to the left region. This scatter can be primarily attributed to the motion of the vortex itself which can be described as eccentric or precessional. Thus, at times with the present set-up the propagating ultrasound beam is blocked by the air-water interface of the moving vortex. When this occurs, the beam is generally scattered in many directions and at the same time, data points comprising the rear one-half of the beam's chord length (when there is intereference) is lacking. As a result, due to large fluctuations in the cumulative velocity signal, a larger and relatively "peaked" SD-distribution is represented. In **Figure 5** we then show V_r at two different axial locations, approximately 5 and 60 mm below the free surface, and their corresponding standard deviations (SD). Note that at this rotation rate the two profiles are only slightly different from each other. This then means that the radial flow is relatively uniform up to 60 mm below the free surface. On the other hand, the SD profiles are different in that for TDX4, 60 mm below the surface, the eccentric motion of vortex is clearly reflected in its profile. Since the ultrasound beam propagates along a chord length, both the "front" and "back" sides of the eccentrically-moving vortex-influenced liquid motion is indicated in the profile as might be expected. Generally speaking, although the velocity profiles as recorded are more difficult to interepret with eccentric motion, the motion itself simulates the expected movement of vortices in a real system. Finally, note that both profiles are not centered because the UVP parameter defining the (data sampling) end channel has been changed.

In **Figure 6** we present the average V_z profile and its SD. This particular profile was taken with the TDX nearly at the side wall. So, it represents the flow along the side wall. It is certain that because the UVP end channel was set at 289 mm, those channels corresponding to (UVP ML ~110-120) represent the bottom of the container. The profile thus shows that from the free surface (ML~0), the flow is (sensibly) downward up to UVP ML~25-30 where there is a steady decrease and subsequent recovery to a quasi-constant value (ML~50 to 70). From ML~70 to 100 then there is another increase with a peak at ML~72. The velocity subsequently decreases to ML~100. It appears that overall there are two major (spatial) regions of flow in any given meridional plane (a cross section) with smaller regions incorporated. The SD-profile equally shows supports this conjecture. The profile steadily increases to a local maxima at ML~60 and subsequently decreases toward ML~100; that is, due to the likely movement of the boundary between the two regions, the SD reaches its largest values there. A sketch of the probable regions of flow in a meridional plane are shown in **Figure 7** along with some of the above-mentioned details.

Next in **Figures 8, 9** and then **10, 11** we present the change in the average and SD-profiles of all 5 TDXs used to measure V_r at 260 and 440 rpms resepctively. One can see that over an axial distance or depth of some 60 mm from the free surface, the radial component of velocity shows relatively little change. This means that over this depth both the radial outflow toward the wall and that near the vortex is relatively uniform. In addition the "on-average" behavior is very much similar. However, the SD-profile, especially at 260 rpm, shows a larger scatter of points even though similar trends are discernable. There are several reasons for this, the first of which may be that at 260 rpm (and lower), the magnetic stirrer itself behaves erratically than at higher rotation rates; that is, at rpms close to 230 rpm the uniformity became uncertain. Thus at 260 rpm any momentary deceleration of the stirrer bar is reflected in the flow. Note too that to the left and right of ML~64 (at 440 rpm; ML~84) there is a clear distinction between two flow regions. That the magnitude of SD first decreases (ML>64) then increases at ML>100 is attributable to eccentric movement of the vortex (air) core near the path of the ultrasound beam as discussed. In contrast, at 440 rpm the region near the edge of the vortex appears relatively well defined by the local maxima (ML~84 and 104). Here due to the steadier rotation rate, the flow field equally exhibits less scatter than at 260 rpm.

Whereas **Fig. 11** depicts the raw SD-profile, in **Figure 12** and **13** show the corresponding *normalized* SD-profiles. In Fig. 12, the SD is normalized by the average velocity, U_{avg} , and in Fig. 13, by the sum of the maximum and minimum velocities, U_{max} and U_{min}. The UVP ML distance has simply been normalized by the total number of measurement channels (128). We see in Fig. 12 that for either normalization method, the relative magnitude of the SD is quasi-constant for $0 < ML < 0.6$. Thereafter, the SD at TDX4 or the corresponding axial distance, $z \sim 60$ mm, exhibits the largest values. This is probably more than coincidence as the profile of the V_z-component also showed a change at about this location (Fig. 6). As for velocity, normalized profiles are not presented because as already noted they only change slightly with TDX position.

Next in **Figures 14, 15** and **16, 17** we show the average velocity and SD profiles, respectively of the V_r- and V_z-components, at various rotation rates. Besides the apparent symmetry in the profile (Fig. 14) we note that consistent with physical intuition, the accelerated central region of velocity widens with an increase in the rotation rate. This trend is also generally followed in the SD profiles as the twin-humped trend describing the eccentric motion-induced flow near the vortex becomes more prominent at higher rpms. The V_z-component in Fig. 16 on the other hand exhibits uniformity except for some deviations at ML~60 and at 88<ML<108. The former of these deviations is likely due to the movement of the regions as mentioned; that is, as indicated in Fig. 7, the relative position of these regions and their contrasting characteristic velocities contribute to scatter in the data. In the latter case as well, there are instances when large axial velocities exist near the bottom of the container and other times when small velocities prevail. This variation certainly contributes to the profile as shown. The flow near the bottom has yet to be investigated in detail.

Since we conducted the experiment by starting at a rotation rate of 230 rpm, incrementally increasing this up to 440 rpm and then incrementally decreasing the rotation rate to 230 rpm (or 260 rpm), in **Figures 18** and **19** we present the average velocity profiles respectively at 260 and 440 rpm for the "up" and "down" sequences. In each figure three profiles are shown because the UVP ML distance in the "up" and "down" phase of the experiment was different such that the profiles appear shifted with respect to each other. We have thus noted the ML location where the maximum velocity was attained in both the "up" and "down" phase and shifted one with respect to the other. We can see that at 260 rpm the profile is nearly identical whereas at 440 rpm, the profiles are slightly displaced even after the max-to-max shift. The gradient of the profile however, is very similar as well as the peak value attained, so that overall we may conclude that both "up" and "down" sequences produced similar flows.

Finally in **Figure 20** we compare velocity and SD profiles of a stirring-induced versus a draining-induced vortical flow. In the latter, the drainage rate out of a 19.8 mm drain line at the bottom of a cylindrical tank (194 mm I.D.) was measured to be 5 *l*/min while the profile shown was measured along the diameter just above the drain hole [13]. We note that while the width of the accelerated regions are slightly different, it appears that these flows with respect to the V_r component are very similar in appearance. The maximum magnitude of the SD on the other hand is larger in the case of the stirring-induced vortex in comparison to the drain-type. This might be expected since we know our vortex precesses (is eccentric), while a drain-type vortex is observed to be steady. In addition at 440 rpm, the "air-core" penetrates much less below the free surface than a drain-type vortex.

3.2.2 2D vector field plots

Two-dimensional vector field plots are presented in **Figures 22** to **25**. The vectors were generated by measurement of V_r and V_z, the former component at five to ten separate locations, depending on whether the transducer was traversed or fixed, and the latter component downward from fixed radial positions at the free surface. A figure of the set-up is first shown in **Figure 21** along with the (Z, R) coordinates, the origin and the distance in [mm] from which the TDX positions were located. The composite vector $V = V_r \mathbf{r} + V_z \mathbf{z}$, where **r, z** are the unit vectors, were calculated at the intersection of the UVP's measurement lines (shown as dotted lines) since we arranged the TDXs to be orthogonal to one another. The V_z-component was typically measured using 4-5 TDXs affixed to a holder with the TDX's front face itself just touching the free surface so that surface tension wetted the front face of the transducer. The V_r-component was measured non-intrusively and as such did not disturb the flow in any way. Hence Fig. 21 shows the merdional (cross-section) plane in which measurements were made. The maximum velocity vector is shown in each vector field plot as a reference vector.

With regards to the calculation of the composite vector, because the active diameter of a transducer is finite (~6mm for 8mm diameter TDX), the actual, imaginary intersection of measurement lines (MLs) is not a point, but rather a "squarish" region roughly 6 x 6 mm^2. In fact, even though the ultrasound beam has a spread angle along its line of propagation (issue addressed below), let us assume that this region is square. So, in order to assign a value to V_z and V_r at the center of this square region, we took the simple arithmetic average across *five* channels centered on the channel nearest the virtual point of intersection.

Figures 22 and **23** respectively show the vector field at 230 and 410 rpm. In both figures, the average vector at 50 spatial points (5 x 10) corresponding to 5 fixed TDXs and one traversing TDX (V_r) set at 10 locations are shown. Strictly speaking since traversing the TDX took time (on the order of 10 minutes), the vector plots shown depict the "on-average" field over this period. As noted a reference vector is located below each vector field plot while the wall region is located at r=140 mm. At a glance several observations and partial conclusions can be drawn as follows.

It is apparent with 50 vectors that localized details of the flow field cannot be elucidated; that is, as Takeda [14] now recommends, upwards of 200 to 300 vectors are needed to reveal relatively small flow regions in a flow field of this size. This then corresponds roughly to a number density of 3 vectors/cm^2. Thus in the present case with a number density of 0.6 vectors/ cm^2 one can only discern the general flow pattern in the present case; that is, as alluded to earlier from 1D plots (example Fig.6) two major flow regions and the region in-between are identifiable. Additionally, the flow near the wall region is mostly axial as it should be and "largely" radial at R~60 mm. Here "largely" means with a larger radial component than an axial component. Surprisingly in Fig. 23 at the lower right hand corner, four vectors identify a local recirculation region while at the upper right, the vectors face a direction contrary to intuition (away from the wall; to the left). It is evident that such peculiarities can only be confirmed or resolved with additional details. This then reveals the limitation with regards to conclusions which can be drawn from these figures. In this respect it is already clear that vectors need to be calculated at more points; that is, additional transducers are needed, finer increments of traverses are required or a combination of both to increase the number of vectors. This is a clear objective of future experiments.

Regarding the error associated with the calculated vectors, due partly to the arrangement of the tranducers (i.e. relative angle; here 90°), partly to the ultrasound acoustics and partly to the nature of the flow, the error associated with each vector is different. First, the transducers in this experiment were arranged orthogonally (at 90° with respect to eachother) so as to ease calculation of $V = V_r \mathbf{r} + V_z \mathbf{z}$. However, since $| V_r | > | V_z|$ in regions close to the vortex core, the relative error associated with the V_z-component is larger than that for the V_r-component. This is accentuated when the velocity approaches the limit of the UVP; that is, as velocities near ~0.7 mm/s. One way to reduce this error is to change the orientation of the transducers with respect to each other so that the larger component of the velocity is included. In the present case, since $| V_r | > | V_z|$, if a "V_z" transducer is oriented to less than 90°, some portion of the larger V_r-component will be included; thus, the relative error should be reduced. The calculation of the vector itself of course only requires measurement of two components.

The error contributions from ultrasound acoustics involve a number of aspects, some of these being: 1) beam spreading, 2) spurious echo signals from multiple reflections and weaker echo signals from channels furthest away from the transducer. Regarding "1)", since the estimated beam spreading angle is 3°, for a beam propagation distance of 14.5 cm (radius of container), the estimate radial spread of the beam is approximately 0.76 cm. Thus the measurement volume of the latter channels (approaching 127 channels) is larger than those in the first few channels. So, potentially the distant channels may contain some bias due simply to a larger measurement volume. These distant channels may also be the source of more multiply-reflected echo signals if the probability of multiple reflections increases with distance from the transducer. The echo signal is of course also weaker from distant channels. The influence of these details have not been investigated as of yet and remains as topics of future investigations. At the moment however, a linearly increased amplification is used by the UVP to compensate for the weaking echo signal with distance.

Finally, the error associated with the flow has already been anticipated. One of the objectives of the test apparatus was to encompass a simple geometry, but a source of "imperfection", meaning movement of the vortex. On the liquid side then this means that the UVP velocity signal will contain vortex motion induced fluctuations in the flow. In fact, one future objective of this experiment is to correlate the movement of a vortex with changes in the 2D flow field. It is thought that both pieces of information may be needed to detect the appearance of a vortex at reactor-scales. Observations of a free surface vortex in a scaled experimental facility have shown that the vortex moves depending on the local flow conditions [15]. At present the signal processing scheme needed to analyze the motion of the vortex using the UVP is not yet established. So, only the on-average 2D vector field has been generated and presented.

Figures 24 and **25** respectively show the "unaveraged" or 1 point-based vector field plot corresponding to Fig. 22 and a direct comparison of the two fields with vectors from each field superimposed on one another. In Fig. 24 then, in contrast to Fig. 22, an average V_z and V_r over *five* (UVP ML) channels are not taken, but instead V_z and V_r values spatially closest to the point of interection (see Fig. 21) have been used to construct the vector. Thus in contrasting the two fields, we note foremost in Fig. 25 that in either case the two major flow regions are similar; that is, the direction and magnitude of the majority of vectors are alike. The vector pairs with apparent differences in magnitude and/or direction are near the free surface (axial Z~280) and in between the regions (axial Z~185). Since on the one hand the vectors in the major regions are alike, supporting a view that the flow is well established in these regions, the contrasting vectors are on the other hand an indication of the spatio-temporal (spce-time) character of these "thin" regions. That is, since the size of the two major regions apparently fluctuates, flow in the vicinity in between these regions may change appreciably. In this case a five "channel" average is obviously more reliable than a one-point value. As for the flow just beneath the free surface it appears that flow is correlated to the relative location of the eccentric vortex with respect to the wall where the TDX is located. This means that when the vortex is accelarated toward the TDX, larger velocities might results; at other instances, a movement away from the TDX may induce smaller velocity flows. The spatio-temporal signal must be investigated to find the exact nature of the correlation between velocity signal and vortex motion.

Lastly in **Figures 26, 27** and **28, 29** we respectively show "banded" grayscale contour maps of the magnitude of velocity and then the vector field superimposed on a contour of the standard deviation of the velocity signal for 230 and 410 rpm. Figs. 26 and 27 have simply been calculated based on $|V| = [V_z{}^2 + V_r{}^2]^{1/2}$ and assigned the same range of grayscale shading for relative comparison purposes. The dark and light tones respectively span a velocity range on the order of 0.7 mm/s (UVP lower limit) to 30 mm/s. Contour plots of this type convey qualitiative information; that is, it is apparent that the spatial distribution of flow regions, whether dark or light, are different at 410 rpm in contrast to 230 rpm. Subsequently when we superimpose a vector plot on a standard deviation contour plot, we arrive at Figs. 28 and 29. Here vectoral information as in Figs. 22-25 is given, but in addition regions where flow fluctuations are large are shown via contours. Again, light tones correspond to larger magnitudes than dark tones.

3.3 Experience with the UVP-X3, 6 TDXs and MPX

The objective of the investigation were two-fold: 1) to demonstrate that a two-dimensional (2D) velocity field, using the ultrasound Doppler velocimeter and a multiple number of ultrasound transducers (6 TDXs in our case), could be measured and 2) to evaluate the content of the measured velocity information with respect to understanding some of the aspects of liquid vortex dynamics.

Our first objective has been fulfilled. Using a total of 6 transducers in various orthogonal arrangements, we measured the V_z and V_r-components of our rotation-induced flow. Measurements were assisted by a multiplexer which acted as a switching device, a PC-based software that controlled the parameters of the multiplexer and finally, the UVP data acquisition software, which was partititoned into 6 blocks (or segments), each consisting of 170 "quasi-instantaneous" profiles. Recall that up to 1024 profiles can be accumulated in the UVP.

Operationally, it is worth noting that the multiplexer is not fast enough to be able to place one profile per block (for 6 TDXs); that is, the time required for switching from transducer to transducer and the "wait" increment necessary to mitigate potential electronic "ringing" from entering the velocity signal as noise, together takes longer than the UVP's data acquisition time for one profile. There is also no cross-talk between the TDXs because only one TDX is triggered at a time and a sufficient "wait" time is given to eliminate any possibility of echoes disturbing the next burst ultrasound pulse. In effect, the user is free to specify five parameters of the multiplexer. Our logic was to synchronize the completion time of both the UVP and the MPX. So, the triggering and wait time were minimized (10 msec and 18 msec respectively), while the "hold" time (18 sec), during which velocity data is recorded, was deemed sufficient for 170 profiles per TDX to be recorded. Only a once-thru cycle (1 cycle) was used with a wait time in-between cycles of 500 msec. More details are given in Appendix B.

4. Conclusions

An experimental investigation was conducted in order to demonstrate that a two-dimensional velocity field could be measured using Met-Flow's Ultrasound Velocity Profile (UVP) monitor, Model X-3 working in conjunction with a JcAir 53/63/64 Multiplexer (MPX). The Model X-3 is currently set-up to operate with up to 20 ultrasound transducers (TDXs) while the MPX esssentially functions as a switching device between the TDX (and thus the experiment) and the X-3 that records the velocity information. The multiplexer is controlled by a software driver that runs on a conventional (IBM-compatible) PC. In the present experiment, up to 6 TDXs were used.

The flow phenomena under study was that of a stirring-induced vortical flow; that is, using a magnetic stirrer (bar; 7.9mm dia x 50.3 mm length) located at the bottom of a cylindrical container (280 mm diameter x 280 mm height), the rotation of the bar was sufficient to induce an air-core vortex at the free surface. Water was the test medium at room temperature conditions. Using 6 TDXs, typically five fixed at the free surface to measure the axial component of the velocity vector, $V = V_r \mathbf{r} + V_z \mathbf{z}$, where **r, z** are the unit vectors, while vertically (z-direction) traversing the TDX measuring the V_r-component, a 2D vector field plot of the flow was subsequently produced by calculating the vector at the spatial intersection (virtual) of the ultrasound beam. The vector plot itself represents the average flow conditions during a 10 minute measurement time.

The following conclusions were either demonstrated or drawn upon.

1) The realization of measuring the components of a velocity vector field using the UVP Model X-3, a multiplexer with PC-driven controller and a multiple number of TDXs was demonstrated.

2) The vector field plots of the upper corner region (within a meridional plane) of a stirring-induced vortical flow in a cylindrical container were generated.

3) Care must be exercised in averaging schemes used to calculate the vector $V = V_r \mathbf{r} + V_z \mathbf{z}$. In other words, extensive cross checking and as well as common sense should be used.

4) It is possible to capture the 2D vector field of slowly varying transients, phenomena that change on the order of 10 minutes or greater with this method.

5) The error associated with each calculated vector is different because of the (spatial) error distribution along the ultrasound beam. In addition, a substantial error can be introduced if one component of the vector is much smaller than the other. This means that the relative angle between the tranducer arrays, which was orthogonal in the present case (90°), should be acute (<90°) or obtuse (>90°) so that both measured components are appreciably larger than its associated error.

6) In our case the magnitude of the V_z -component is small so that the error is larger than that of the V_r-component. The transducers used for the V_z -component should thus be oriented (<90°) to include some part of the V_r-component. This will be done in a future experiment.

Nomenclature

ML: Measurement Length, refers to UVP measurement length

SD: Standard Deviation of the average

TDX: refers to ther ultrasound transducer

$U_{avg.}$ $U_{max,}$ U_{min}: Average velocity at the entrance of test section

V_r, V_z : Radial and axial components of velocity

V: Velocity vector, ($V= V_r \mathbf{r} + V_z \mathbf{z}$)

u', v' : Fluctuating component of velocity

r, z: Radial and axial directions; also unit vectors

List of References

[1] R.H.S. Winterton, Cover-gas bubbles in recirculating sodium primary circuit, Nucl. Eng. Des., 22, 262-271, 1972.

[2] J. S. Schetz and A. E. Fuhs, Eds., Handbook of fluid dynamics and fluid machinery, Vol. III, John Wiley and Sons, New York, USA, 1996.

[3] E. P. Rood and J. Katz, Free-Surface Turbulence, ASME-FED Summer Mtg., Lake Tahoe, Nevada, USA, Jun3 19-23, 1994

[4] M. Iida, Free surface flow analysis by fluid dynamic code SPLASH-ALE - Self-induced oscillation of upward plane jet-, Fall Mtg. Atomic Energy Soc. Japan, Tohoku Univ., Sendai, Japan, Sept. 23-25, no. C26, 335, 1996.

[5] Y. Dolias, notes and private communication, 1996.

[6] K. Okamoto, Particle image velocimetry around the vortex dimple at free surface, J. Flow Visualization Image Processing, 1, 347-358, 1993.

[7] JcAir 53/63/64 multiplexer, 400 Industrial Parkway, Industrial Airport, Kansas, USA 66031.

[8] Ultrasound Velocity Profile monitor (UVP), Model X-3, Met-Flow SA, Lausanne, Switzerland, 1992.

[9]Y. Takeda, Velocity profile measurement by ultrasound Doppler shift method, Int. J. Heat and Fluid Flow, vol. 7, 313-318, 1986.

[10] Y. Takeda, Measurement of velocity profile of mercury flow by ultrasound Doppler shift method, Nuclear Technology, 79, 120, 1987.

[11] Y. Takeda, Development of an ultrasound velocity profile monitor, Nucl. Eng. Design, vol. 126, 277-284, 1990.

[12] Y. Takeda, K. Samec and K. Kobayashi, Experimental measurement of 2D velocity vector field using ultrasonic velocity profile monitor (UVP), ASME FED-128, Experimental and Numerical Flow Visualization, 231, 1991.

[13] S. Sakai, H. Madarame and K. Okamoto, Flow distribution around a bathtub vortex, Proc. 3rd. JSME/ASME Joint. Int. Conf. Nucl. Eng., S-124-2, April 23-27, Kyoto, Japan 1995.

[14] Y. Takeda, private communication, 1997.

[15] Visit to CRIEPI, 1996.

Acknowledgements

The first author would like to thank PNC for his appointment as PNC International Fellow.

Appendix A
Ultrasound Doppler principles and UVP operational parameters.

Ultrasound Doppler velocimetry

- Principle works on ultrasound (acoustical) echography; time-of-flight measures position; Doppler shift enables calculation of velocity; sign of Doppler shift indicates direction of flow.
- Ultrasound transducer is pulsed; ultrasound is reflected from tracer-particles;tracer particles are added in to water; in sodium, *impurities* act as tracer-particles.
- Velocity profile is constructed along 128 points; magnitude and sign.
- 1024 profiles are taken during each measurment run.

Spatio-temporal velocity data is recorded.

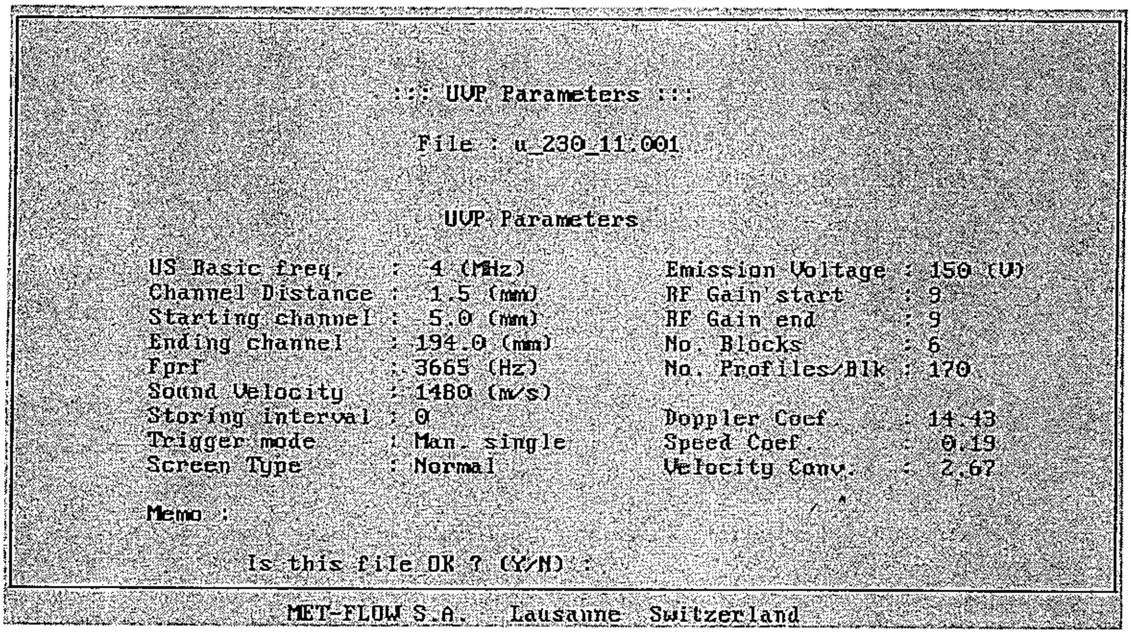

```
                    ::: UVP Parameters :::

                     File : u_230_11.001


                      UVP Parameters

US Basic freq.    :  4 (MHz)          Emission Voltage : 150 (V)
Channel Distance  :  1.5 (mm)         RF Gain start    : 9
Starting channel  :  5.0 (mm)         RF Gain end      : 9
Ending channel    : 194.0 (mm)        No. Blocks       : 6
Fprf              : 3665 (Hz)         No. Profiles/Blk : 170
Sound Velocity    : 1480 (m/s)
Storing interval  : 0                 Doppler Coef.    : 14.43
Trigger mode      : Man. single       Speed Coef.      :  0.19
Screen Type       : Normal            Velocity Conv.   :  2.67

Memo :

        Is this file OK ? (Y/N) :

           MET-FLOW S.A.   Lausanne  Switzerland
```

Figure A-1.Typical UVP operational parameters used in this work

Appendix B

Diagram of UVP-X3 multiplexer parameters

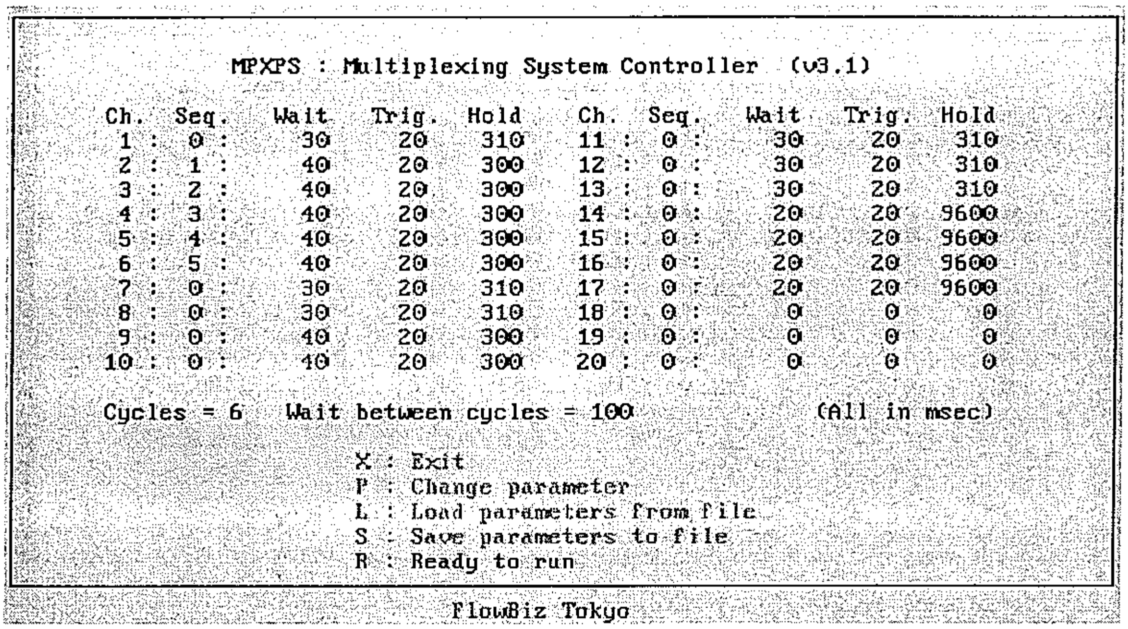

```
              MPXPS : Multiplexing System Controller  (v3.1)

  Ch.  Seq.    Wait   Trig.  Hold     Ch.  Seq.    Wait   Trig.  Hold
   1 :  0 :     30     20     310     11 :  0 :     30     20     310
   2 :  1 :     40     20     300     12 :  0 :     30     20     310
   3 :  2 :     40     20     300     13 :  0 :     30     20     310
   4 :  3 :     40     20     300     14 :  0 :     20     20    9600
   5 :  4 :     40     20     300     15 :  0 :     20     20    9600
   6 :  5 :     40     20     300     16 :  0 :     20     20    9600
   7 :  0 :     30     20     310     17 :  0 :     20     20    9600
   8 :  0 :     30     20     310     18 :  0 :      0      0       0
   9 :  0 :     40     20     300     19 :  0 :      0      0       0
  10 :  0 :     40     20     300     20 :  0 :      0      0       0

  Cycles = 6   Wait between cycles = 100               (All in msec)

                        X : Exit
                        P : Change parameter
                        L : Load parameters from file
                        S : Save parameters to file
                        R : Ready to run
                             FlowBiz Tokyo
```

Figure B-1. Diagram of MPX operational parameters.

Appendix C

Typical gray-scale, magnitude encoded velocity profile image

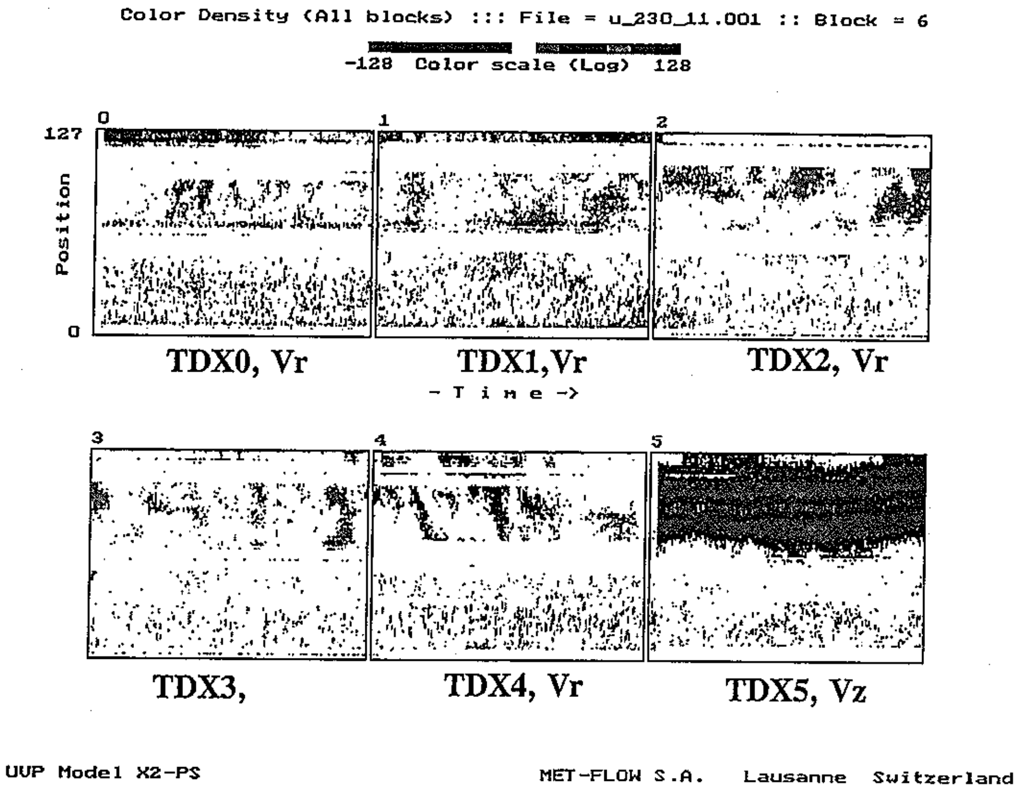

Figure C-1. Typical gray-scale, magnitude encoded velocity profile image. Velocity profiles of our 6 TDXs from top left to bottom right.

Appendix D

Schematic of experimental apparatus

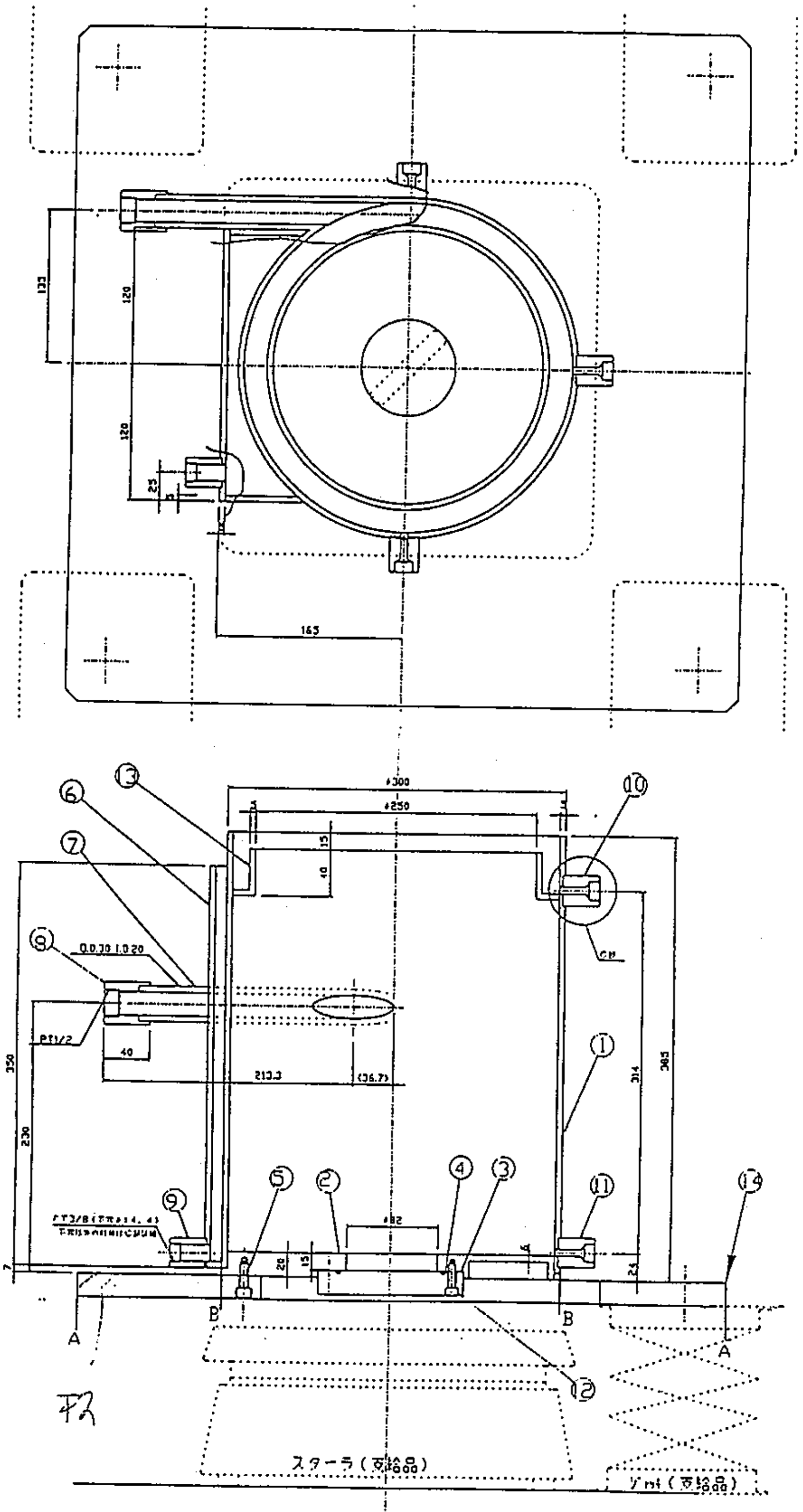

Figure D-1. Schematic of experimental apparatus.

Appendix E

Information sheet on Expancel tracer particle used in the experiment

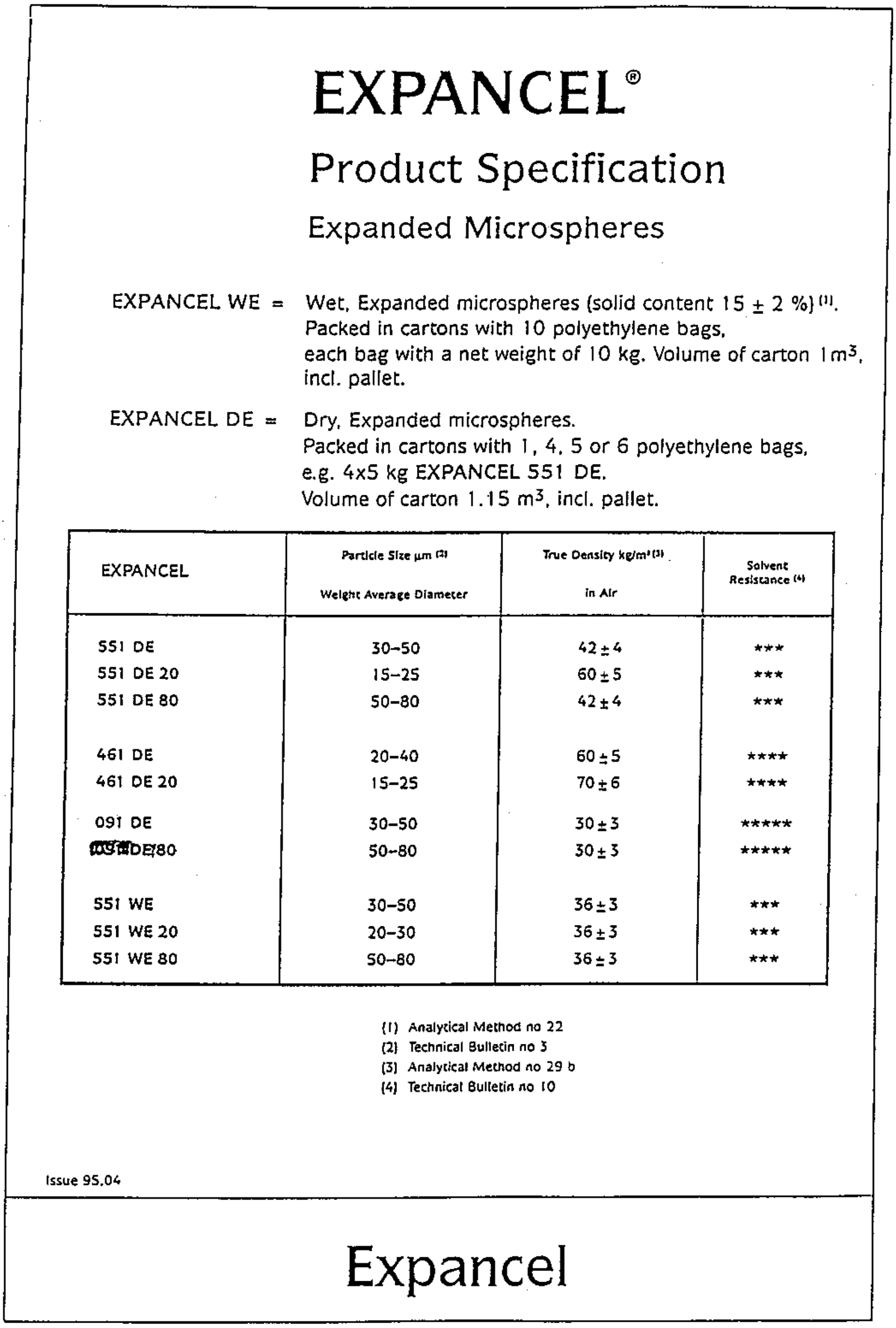

EXPANCEL®

Product Specification

Expanded Microspheres

EXPANCEL WE = Wet, Expanded microspheres (solid content 15 ± 2 %)(1).
Packed in cartons with 10 polyethylene bags,
each bag with a net weight of 10 kg. Volume of carton 1 m^3,
incl. pallet.

EXPANCEL DE = Dry, Expanded microspheres.
Packed in cartons with 1, 4, 5 or 6 polyethylene bags,
e.g. 4x5 kg EXPANCEL 551 DE.
Volume of carton 1.15 m^3, incl. pallet.

EXPANCEL	Particle Size µm (2) Weight Average Diameter	True Density kg/m^3 (3) in Air	Solvent Resistance (4)
551 DE	30–50	42 ± 4	***
551 DE 20	15–25	60 ± 5	***
551 DE 80	50–80	42 ± 4	***
461 DE	20–40	60 ± 5	****
461 DE 20	15–25	70 ± 6	****
091 DE	30–50	30 ± 3	*****
091 DE 80	50–80	30 ± 3	*****
551 WE	30–50	36 ± 3	***
551 WE 20	20–30	36 ± 3	***
551 WE 80	50–80	36 ± 3	***

(1) Analytical Method no 22
(2) Technical Bulletin no 3
(3) Analytical Method no 29 b
(4) Technical Bulletin no 10

Issue 95.04

Expancel

Figure E-1. Information sheet on Expancel tracer particle used in the experiment.

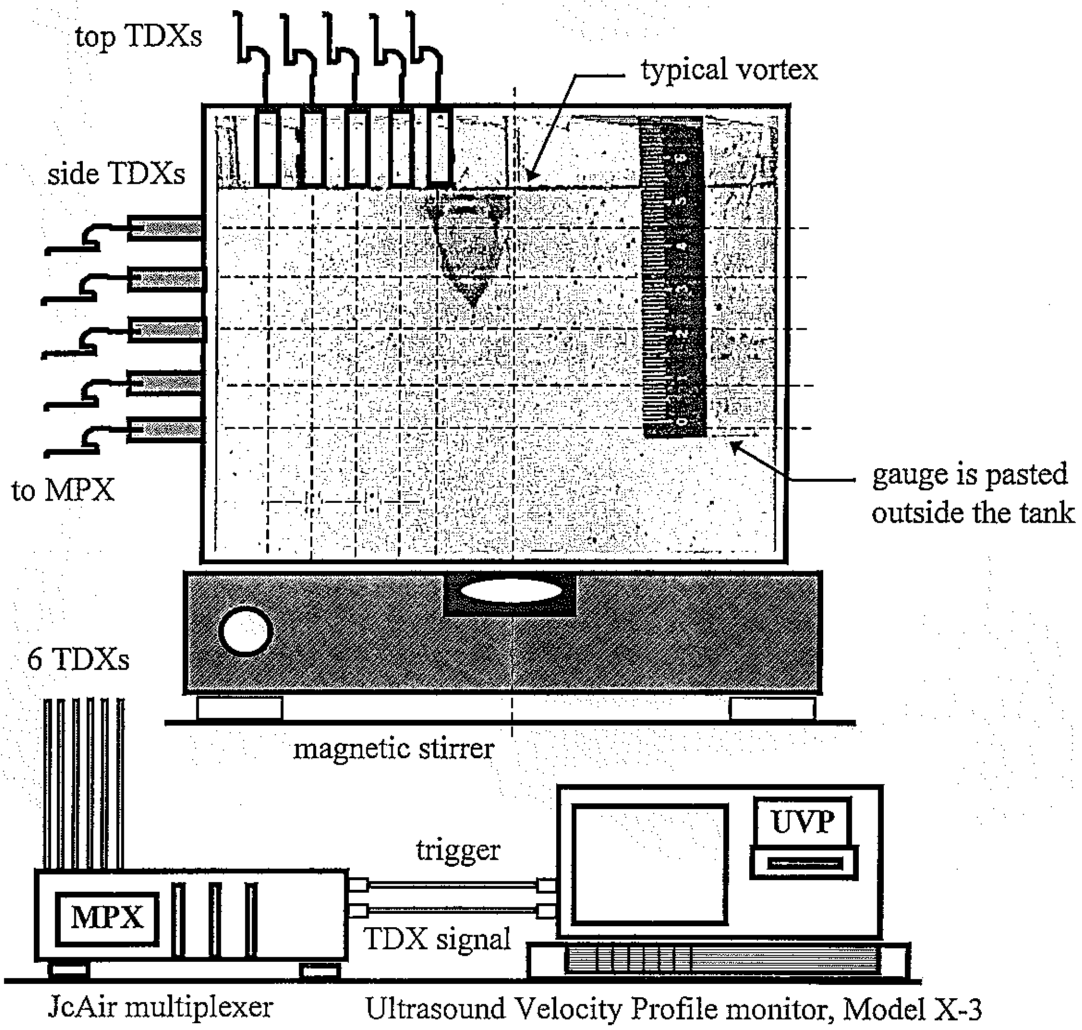

Figure 1. Schematic of experimental set-up showing tank, magnetic stirrer, multiplexer (MPX) and UVP, Model X-3.

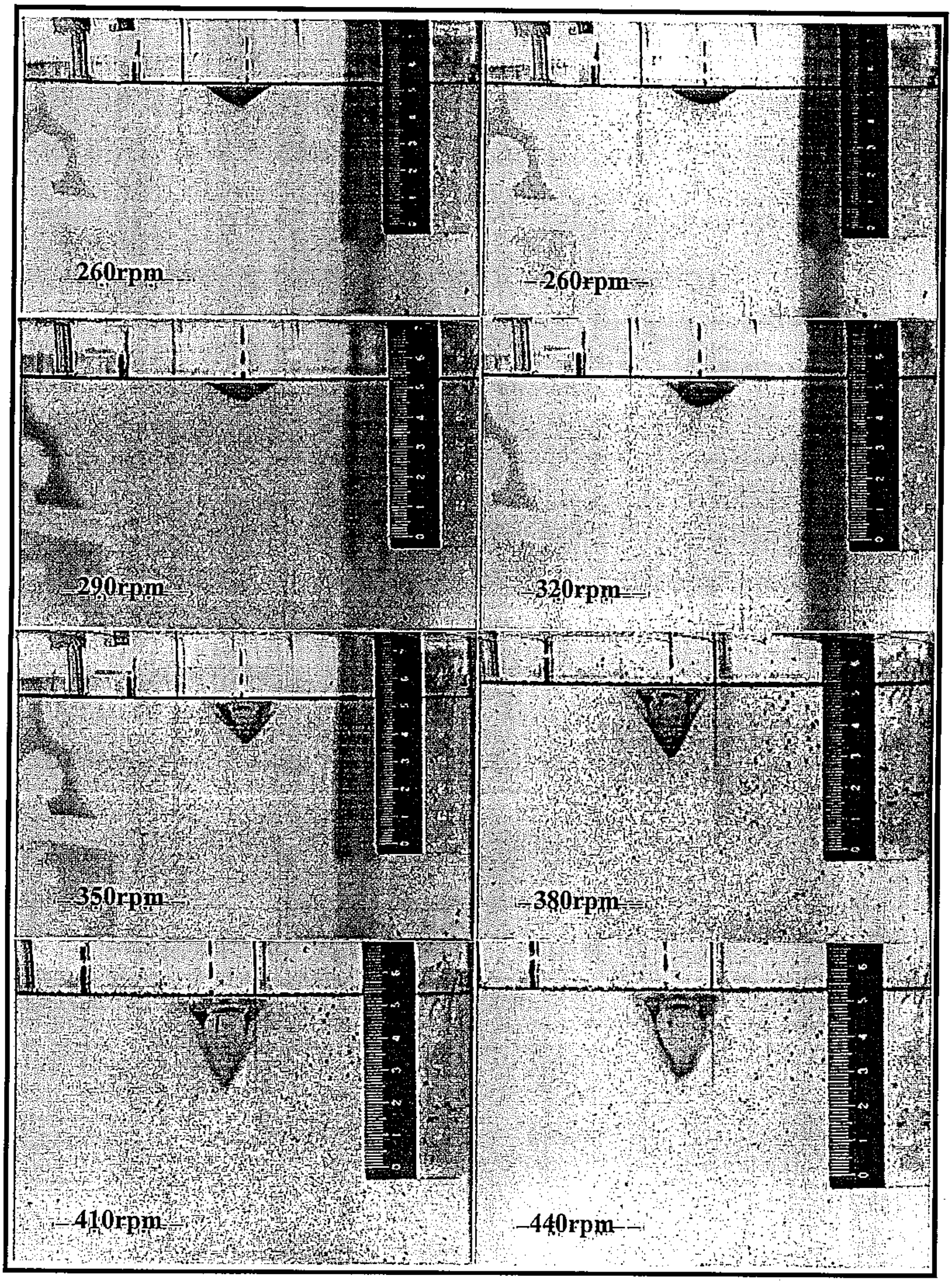

Figure 2. Snapshot images of the swirling vortex generated by a magnetic stirrer located at the bottom of a cylindrical tank. The top two show two different views at 260rpm; thereafter (left-to-right) 290, 320, 350, 380, 410, 440rpm.

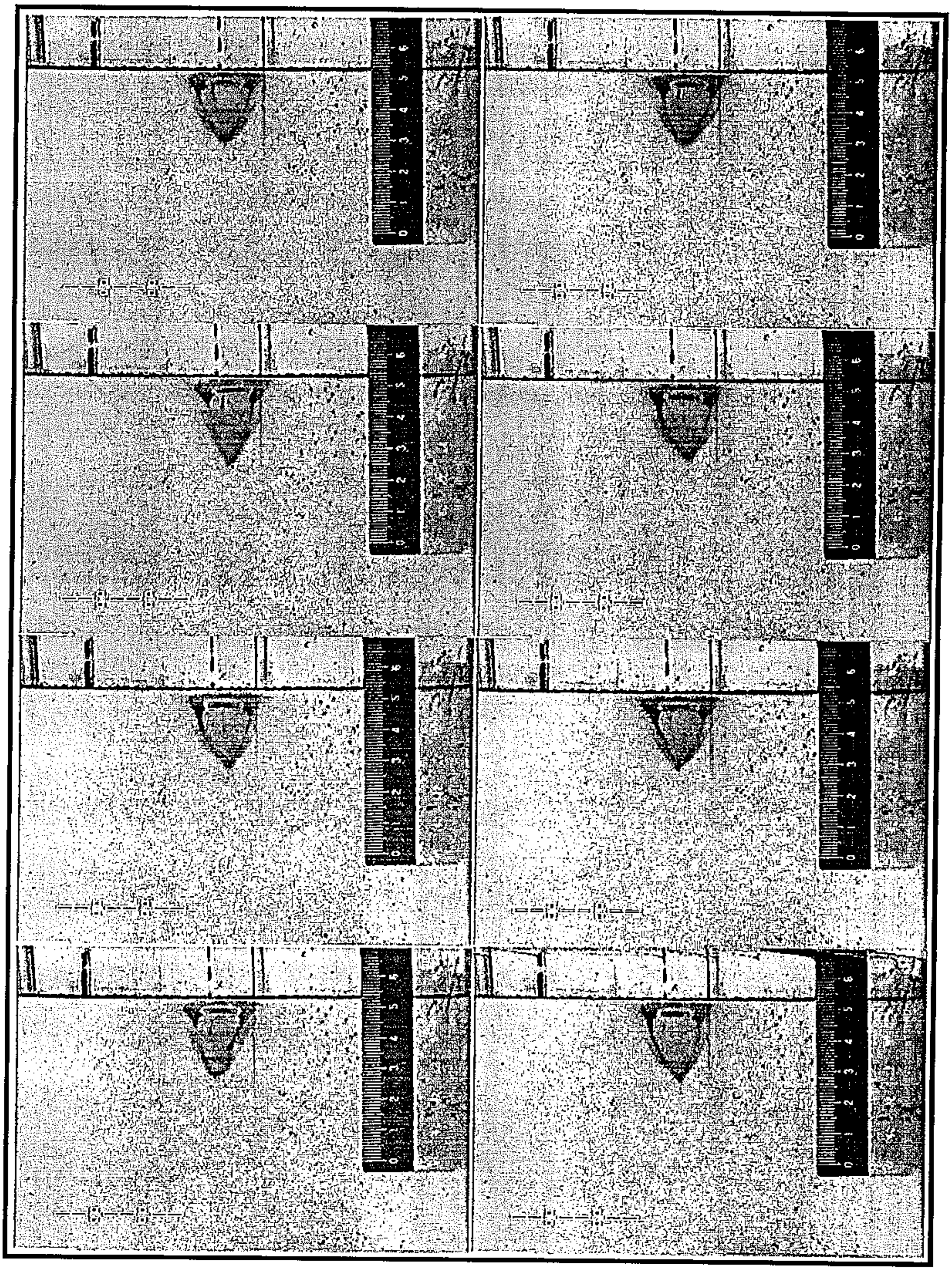

Figure 3. A sequence of snapshot images of the swirling vortex generated by a magnetic stirrer rotating at 410 rpm.

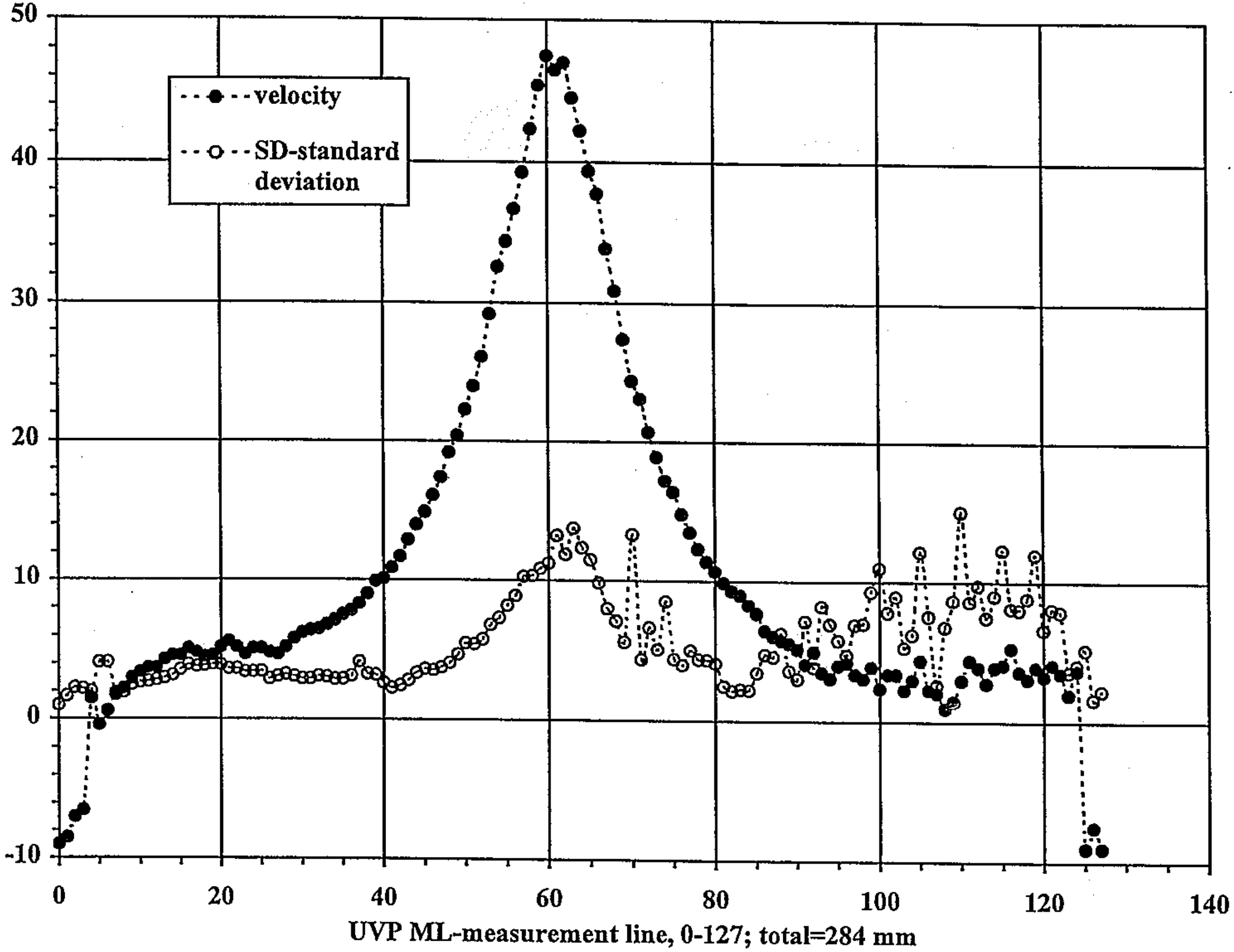

Figure 4. Average velocity and standard deviation profiles of the radial velocity component at 230 rpm. (TDX just below free surface)

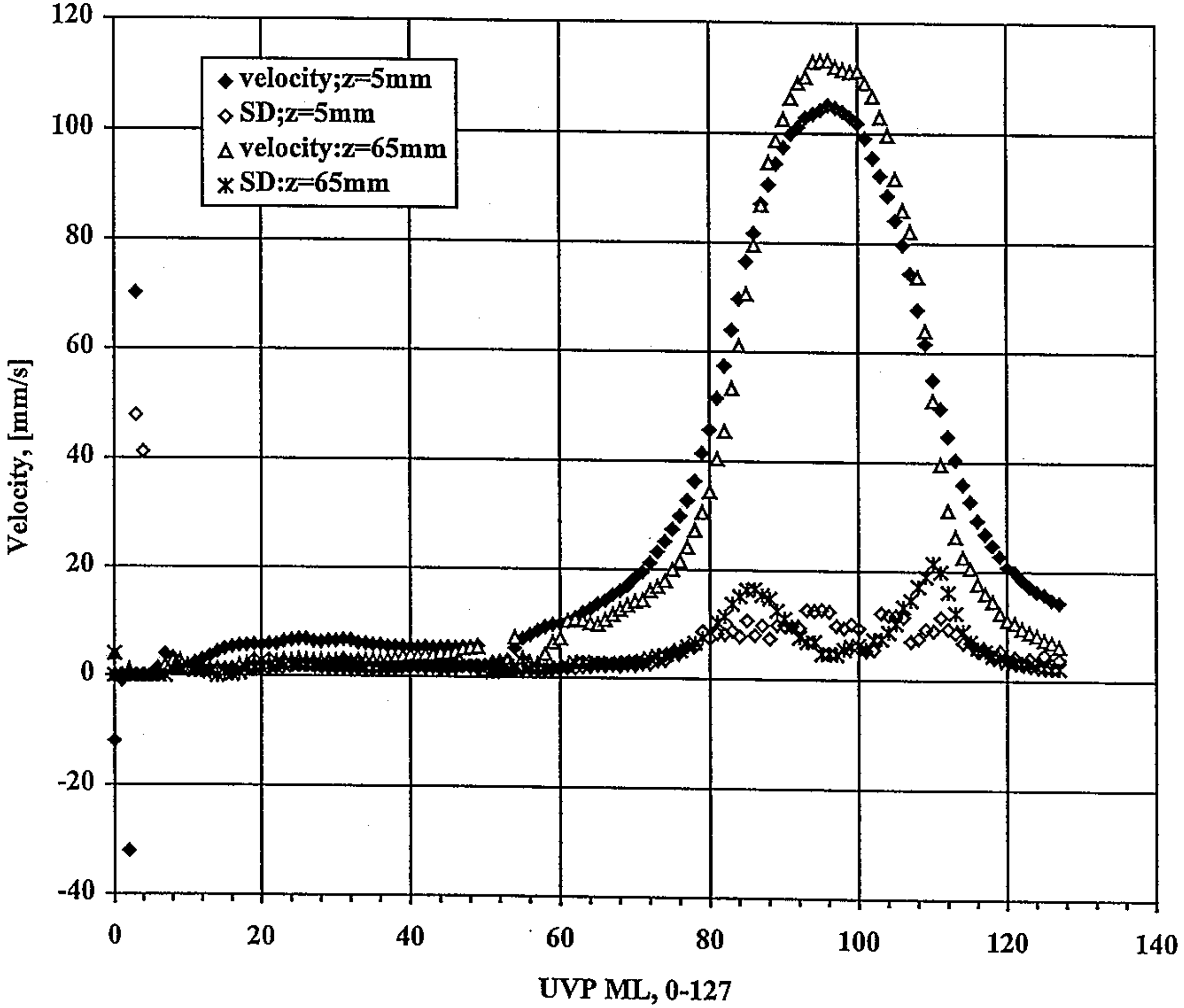

Figure 5. Average velocity and SD profiles of the radial component at 440 rpm.

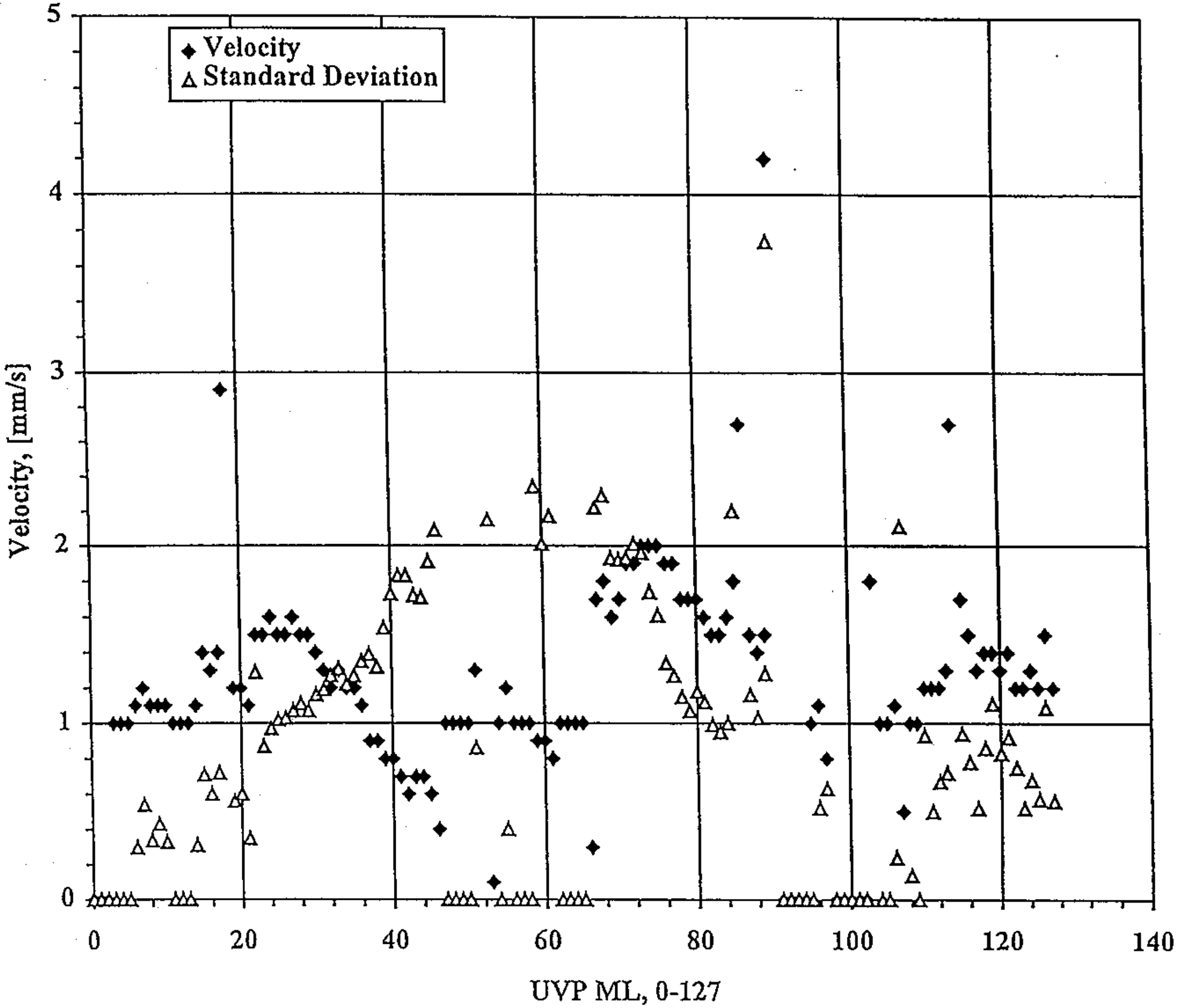

Figure 6. Average velocity and SD profiles of the axial component near the wall at 260rpm.

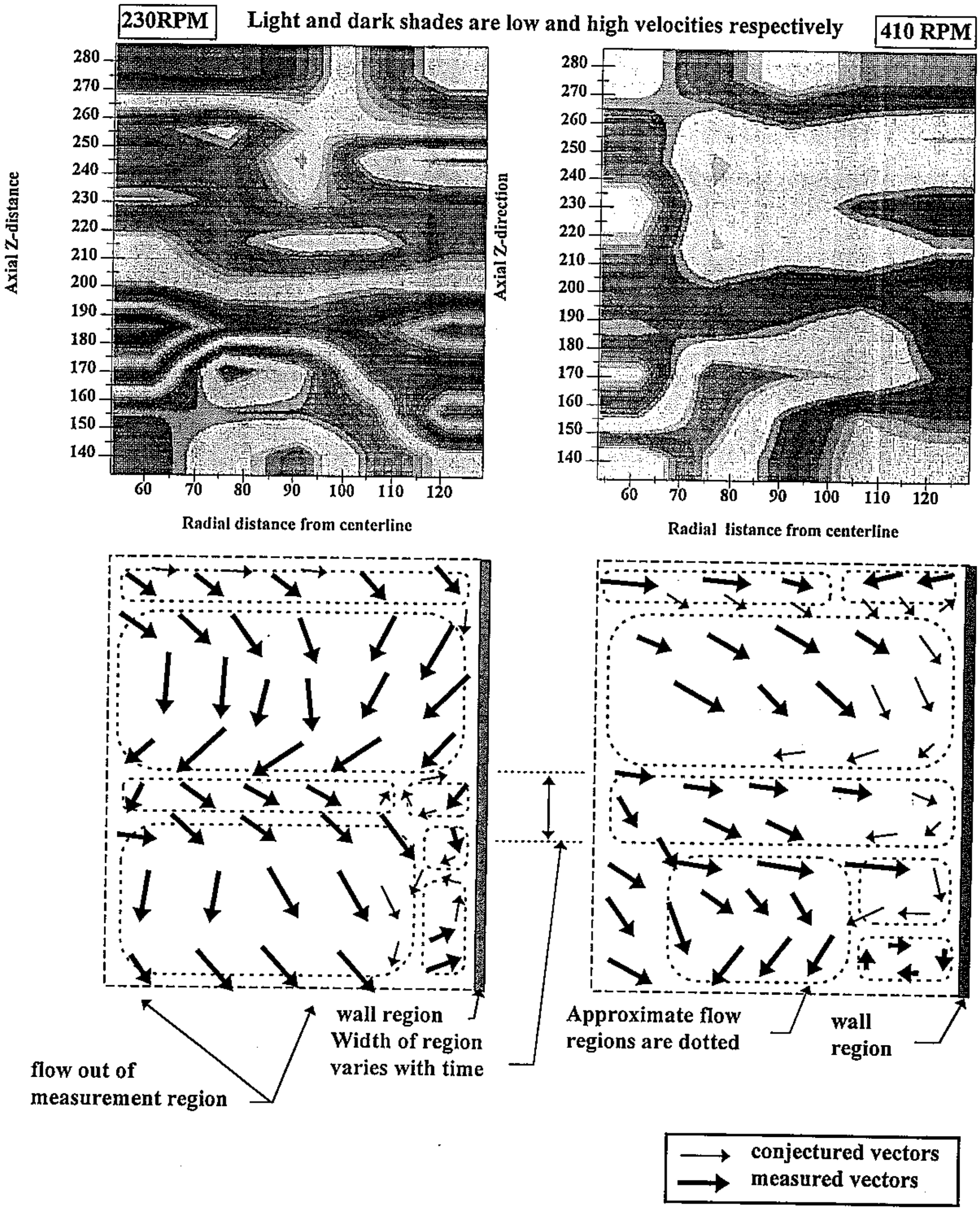

Figure 7. Contours of the magnitude of velocity for rotation rates 230 and 410 rpm and corresponding qualitative sketches of flow regions and their features.

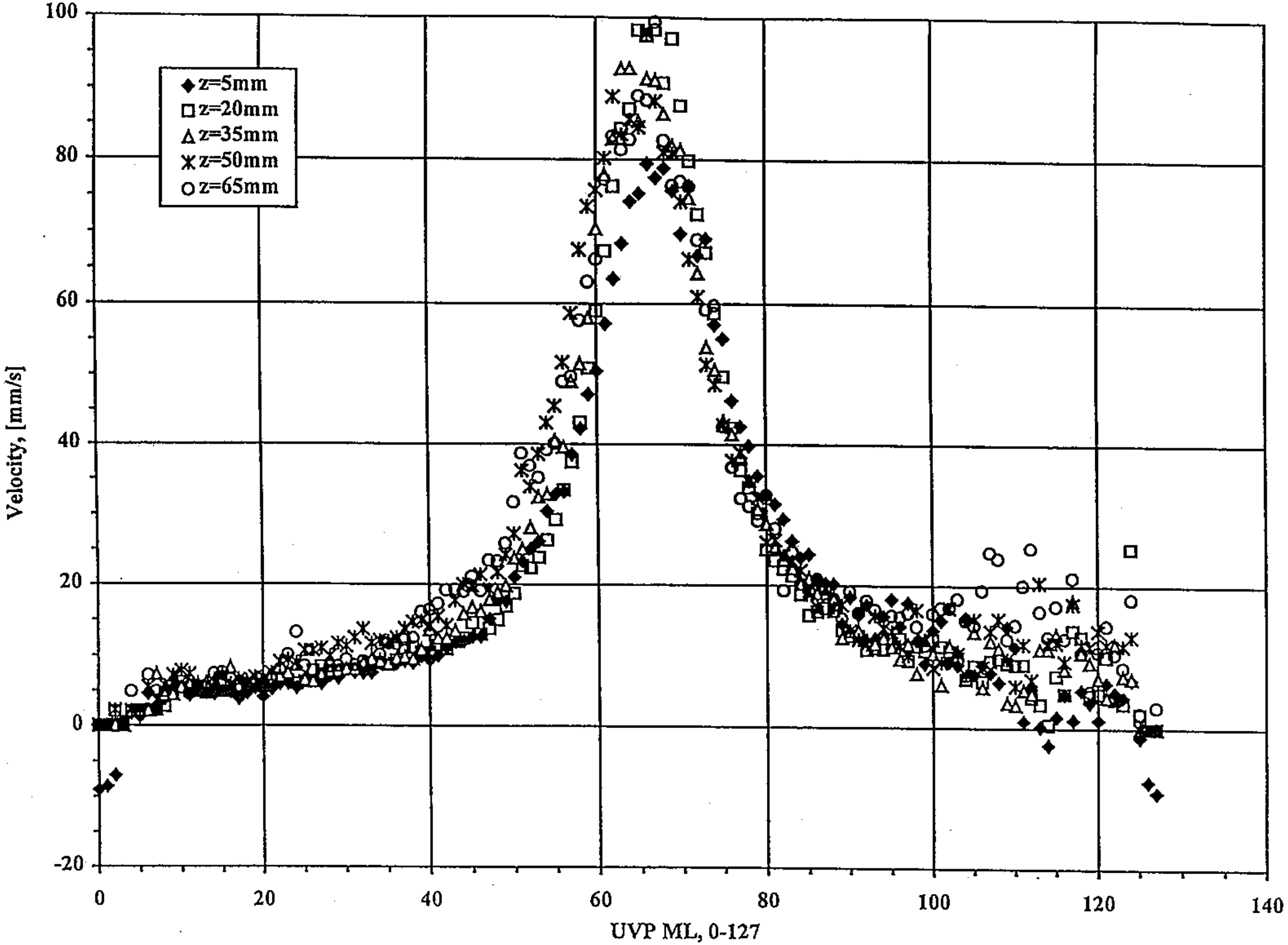

Figure 8. Average velocity profiles of the radial component at 5 axial locations at 260 rpm.

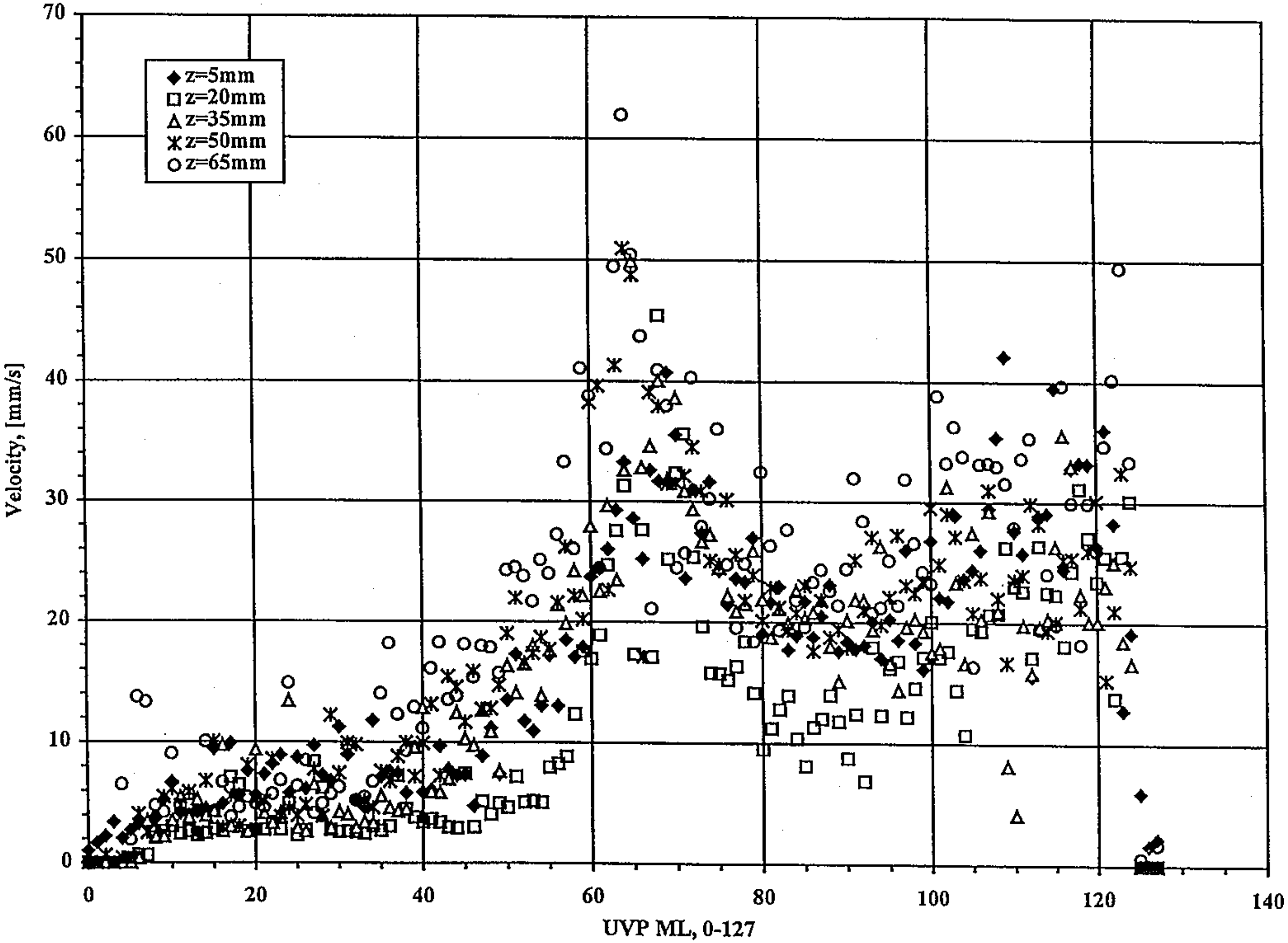

Figure 9. Standard deviation profiles of the radial component at 5 axial locations at 260 rpm.

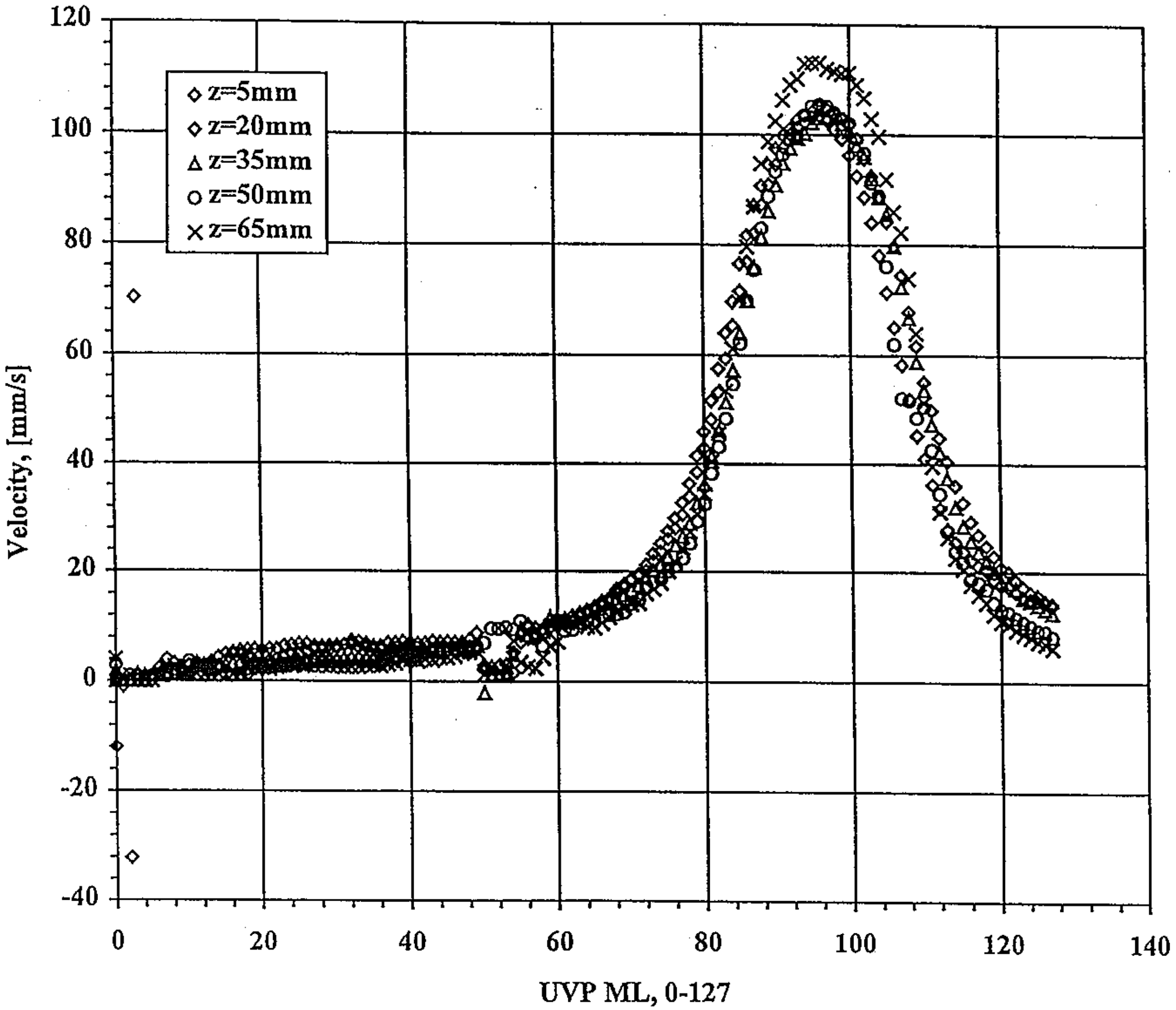

Figure 10. Average velocity profiles of the radial component at 5 axial locations at 440rpm.

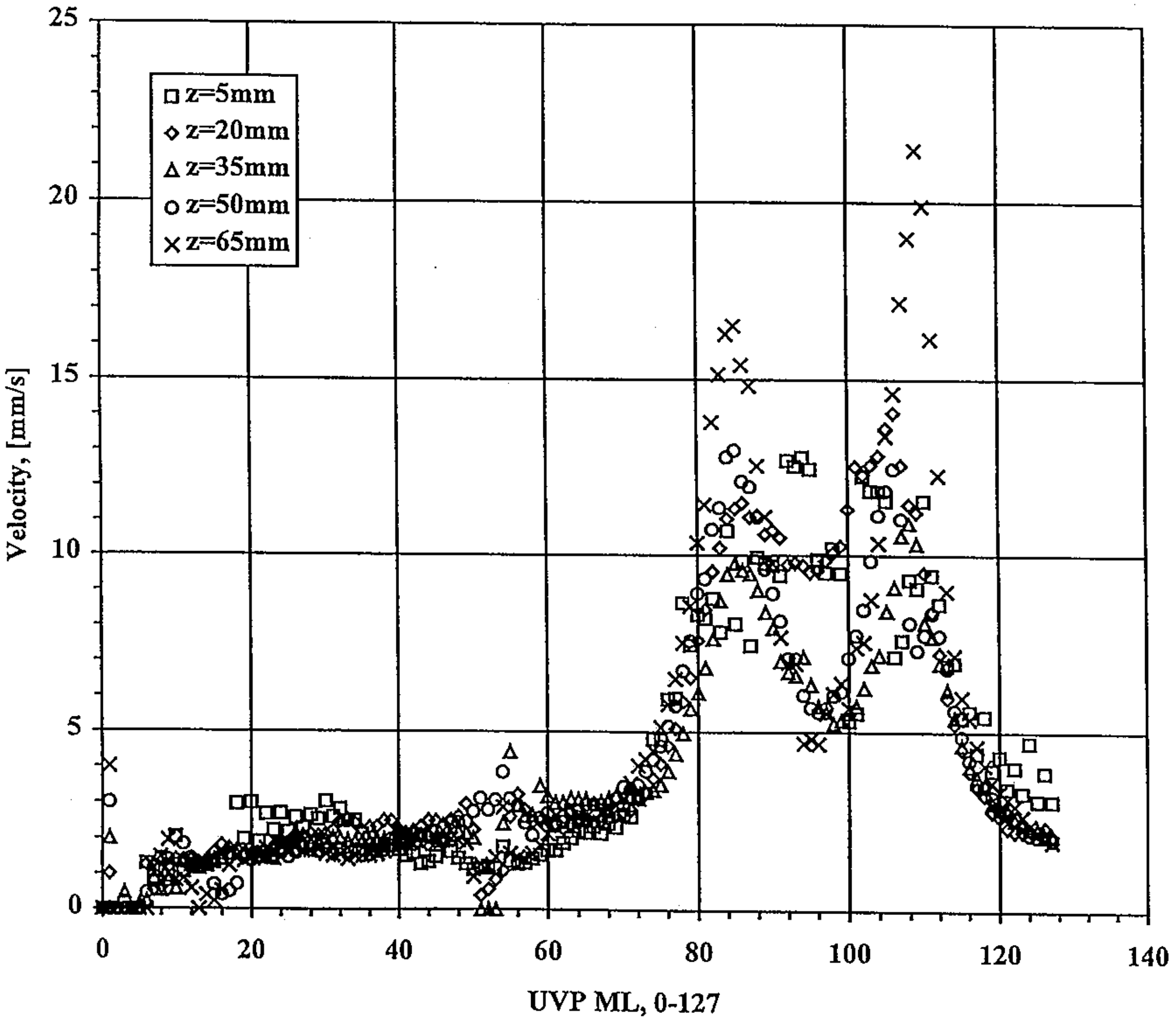

Figure 11. Standard deviation profiles of the radial component at 5 axial locations at 440 rpm.

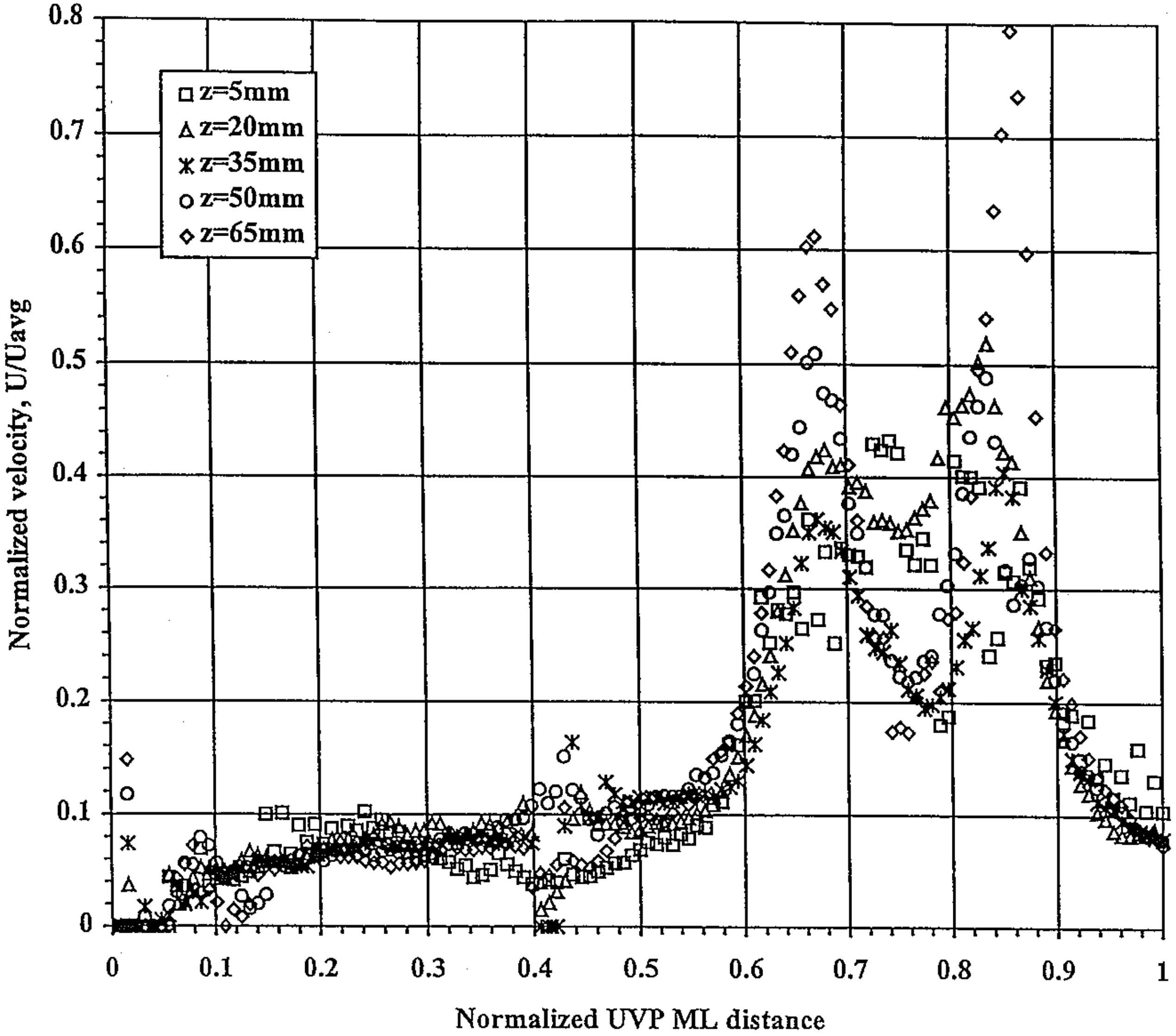

Figure 12. Normalized profiles of the radial SD at 5 radial positions at 440 rpm.

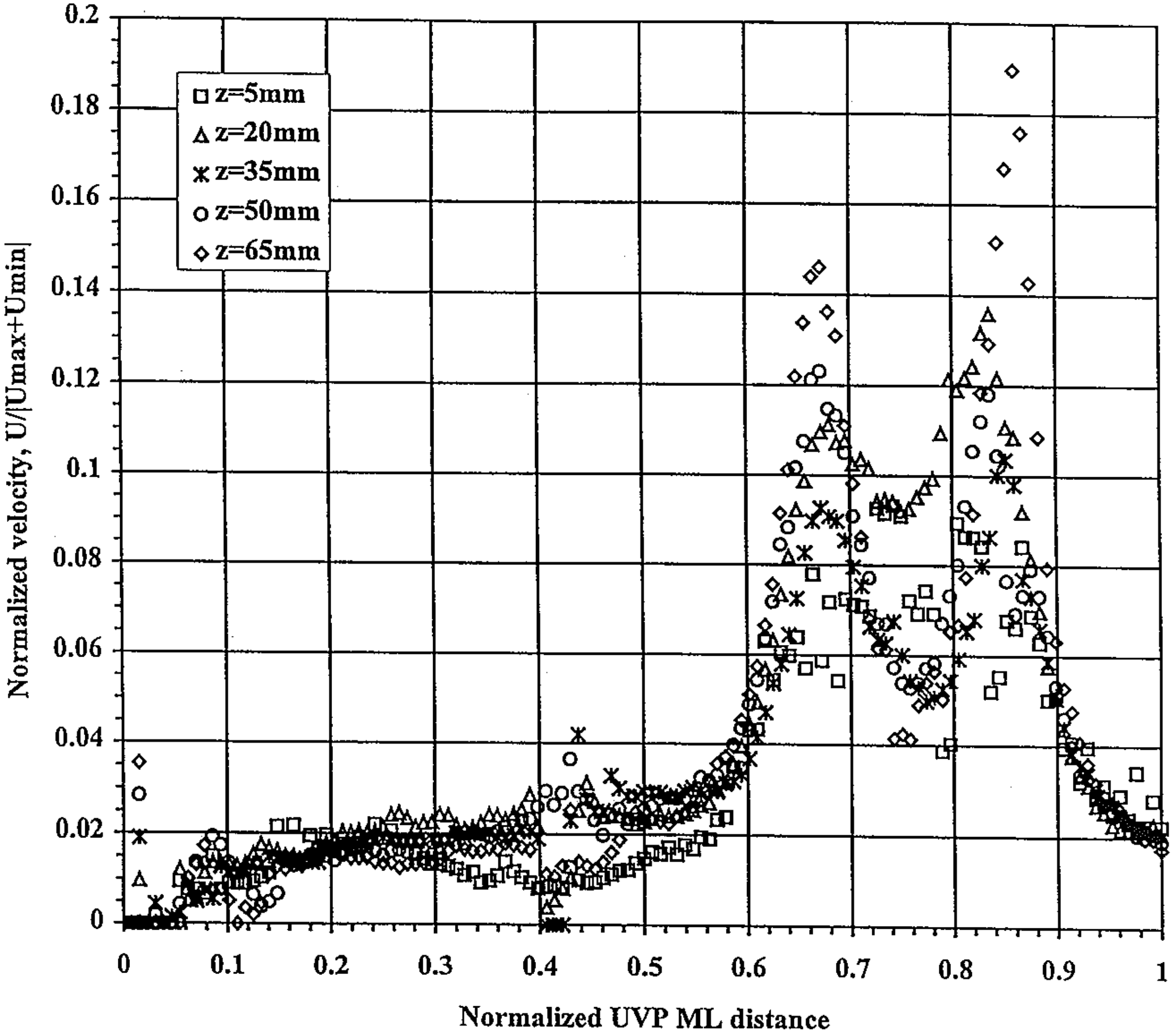

Figure 13. Normalized profiles of the radial SD at 5 axial positions at 440 rpm.

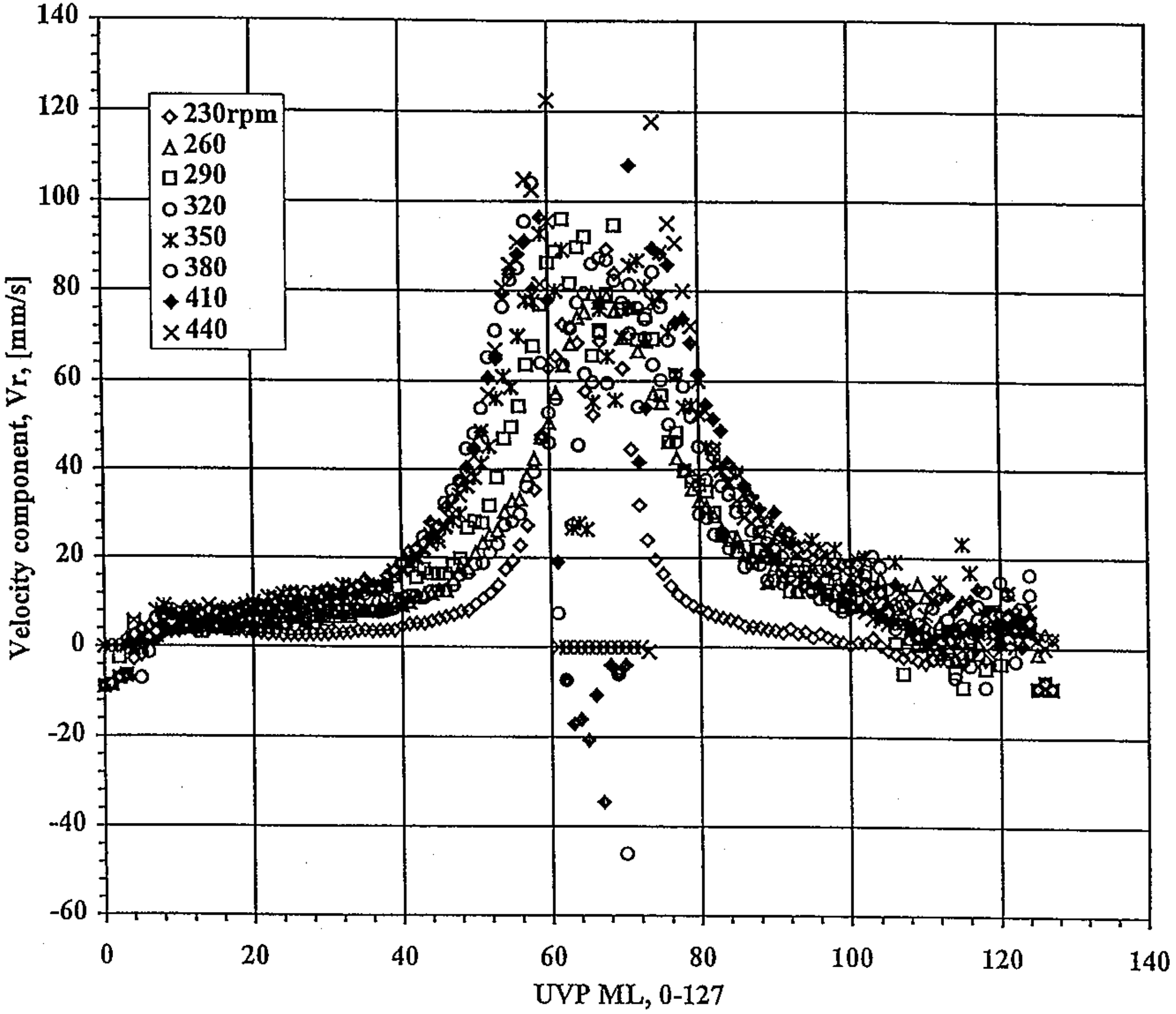

Figure 14. Change in the average velocity profile of the radial component, Vr, at various rpms.

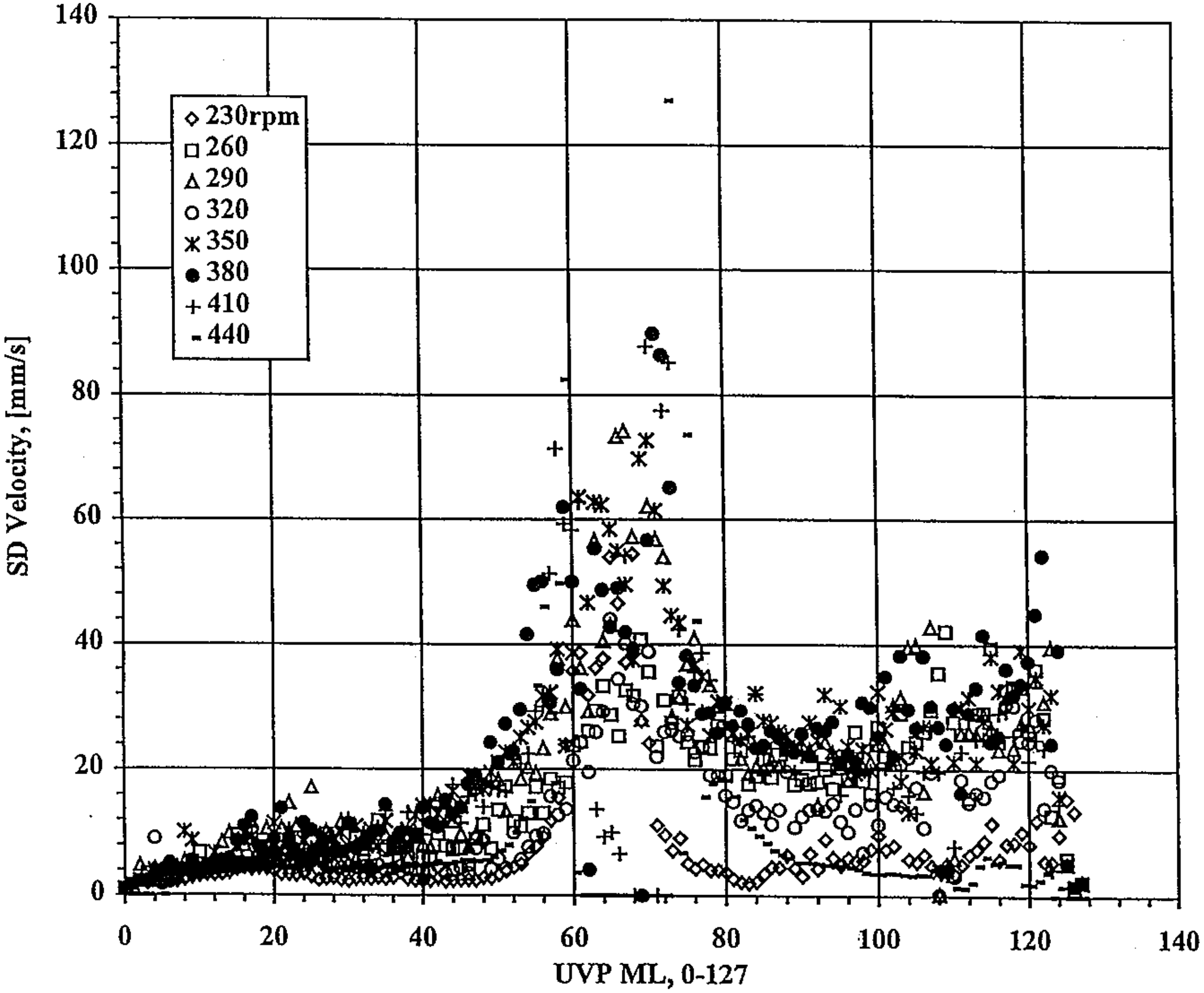

Figure 15. Changes in the SD profile of the radial component, Vr, at various rpms.

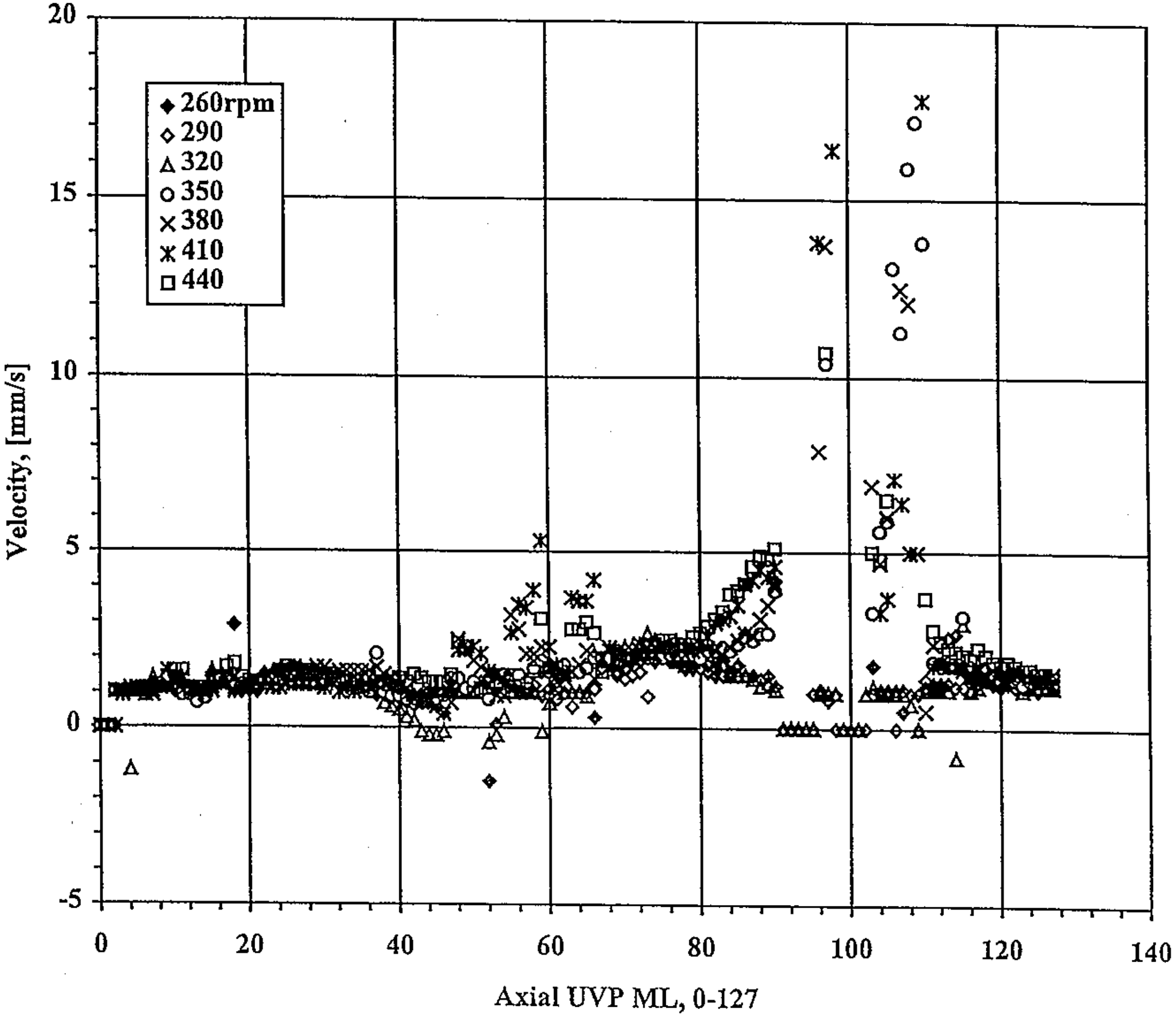

Figure 16. Change in the average velocity profile of the axial component, Vz, at various rpms.

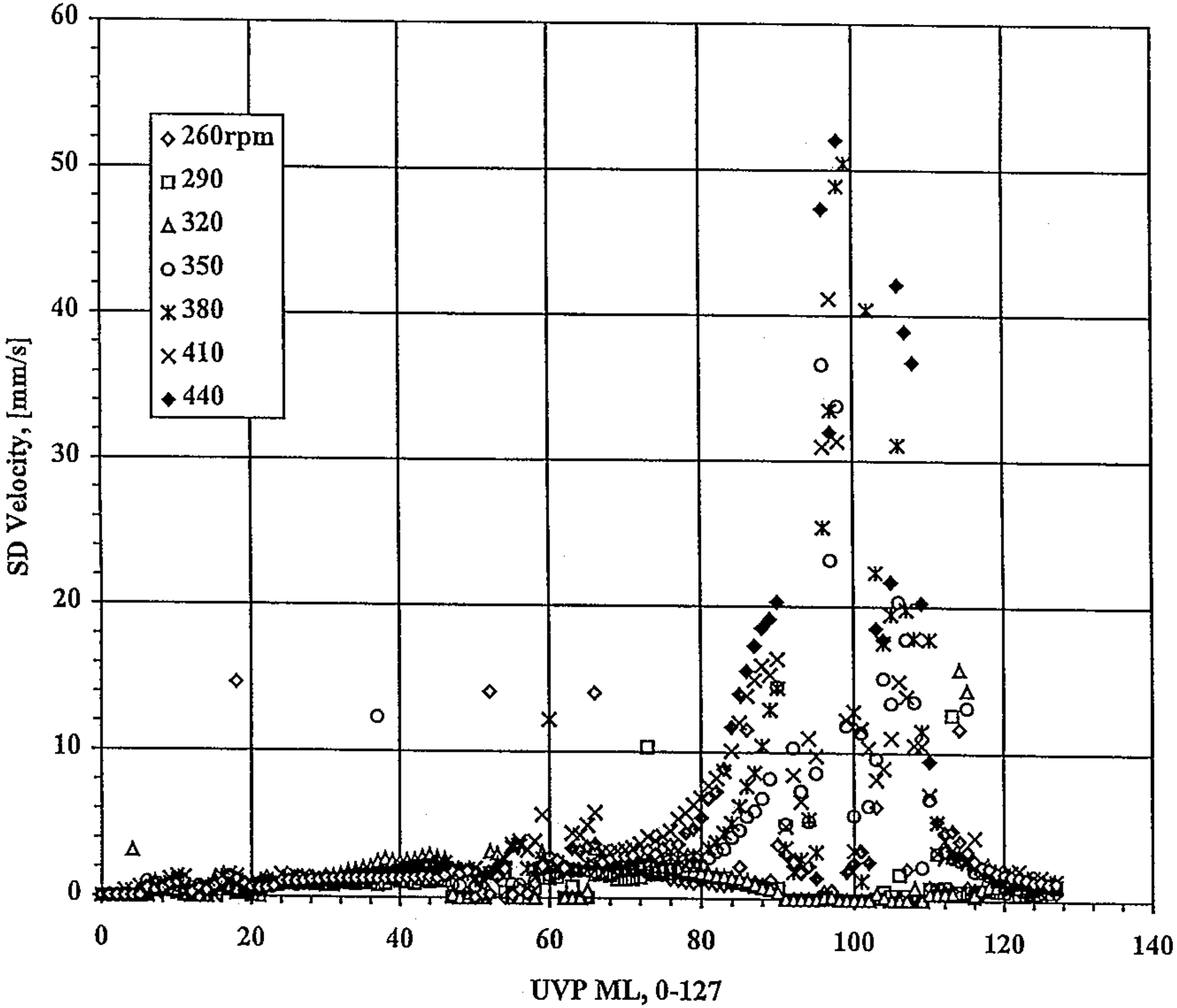

Figure 17. Change in the SD profile of the axial component, Vz, at various rpms.

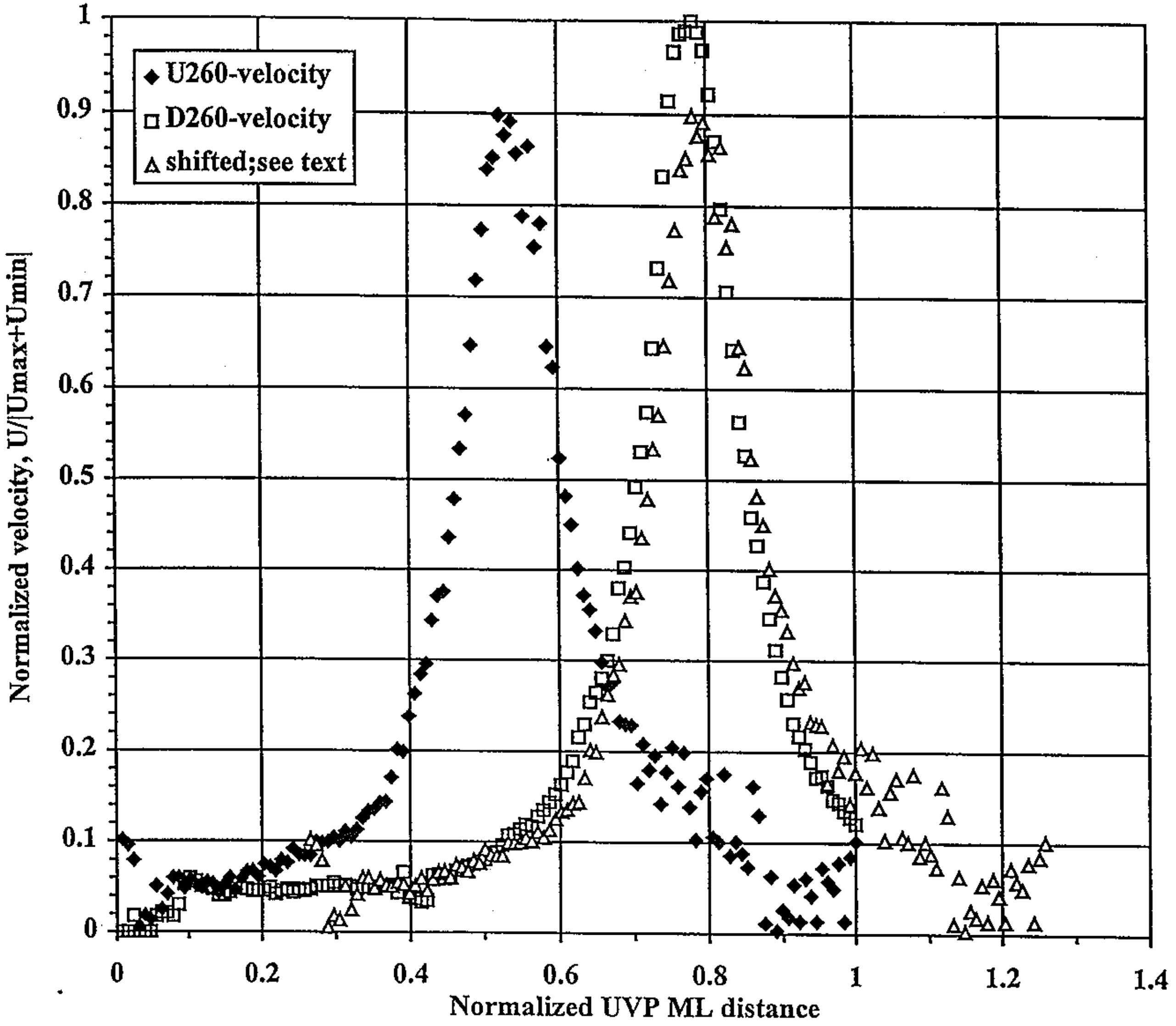

Figure 18. Comparison of the radial velocity component taken in the "up" and "down" phase at 260 rpm.

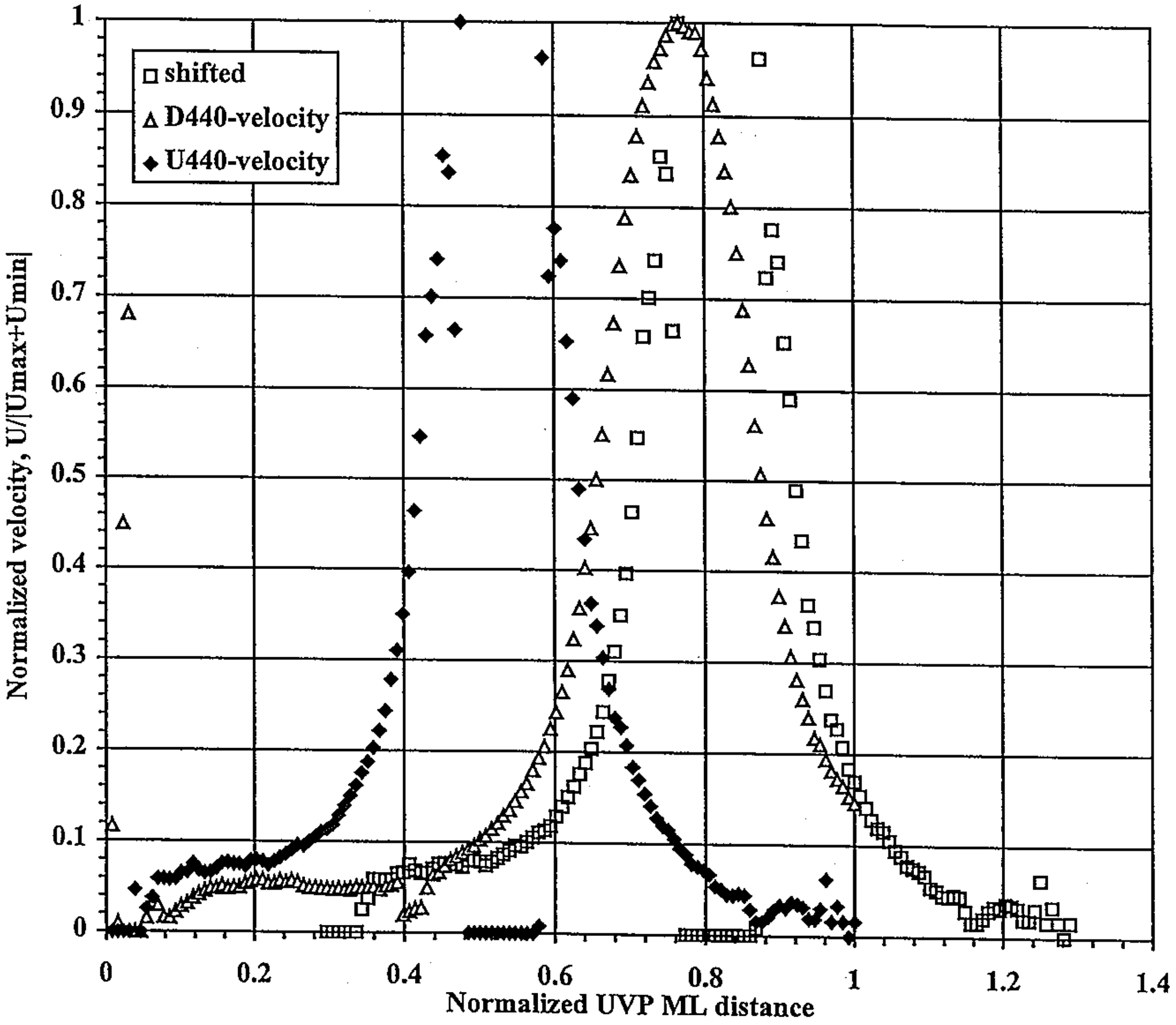

Figure 19. Comparison of the radial velocity component taken in the "up" and "down" phase at 440rpm.

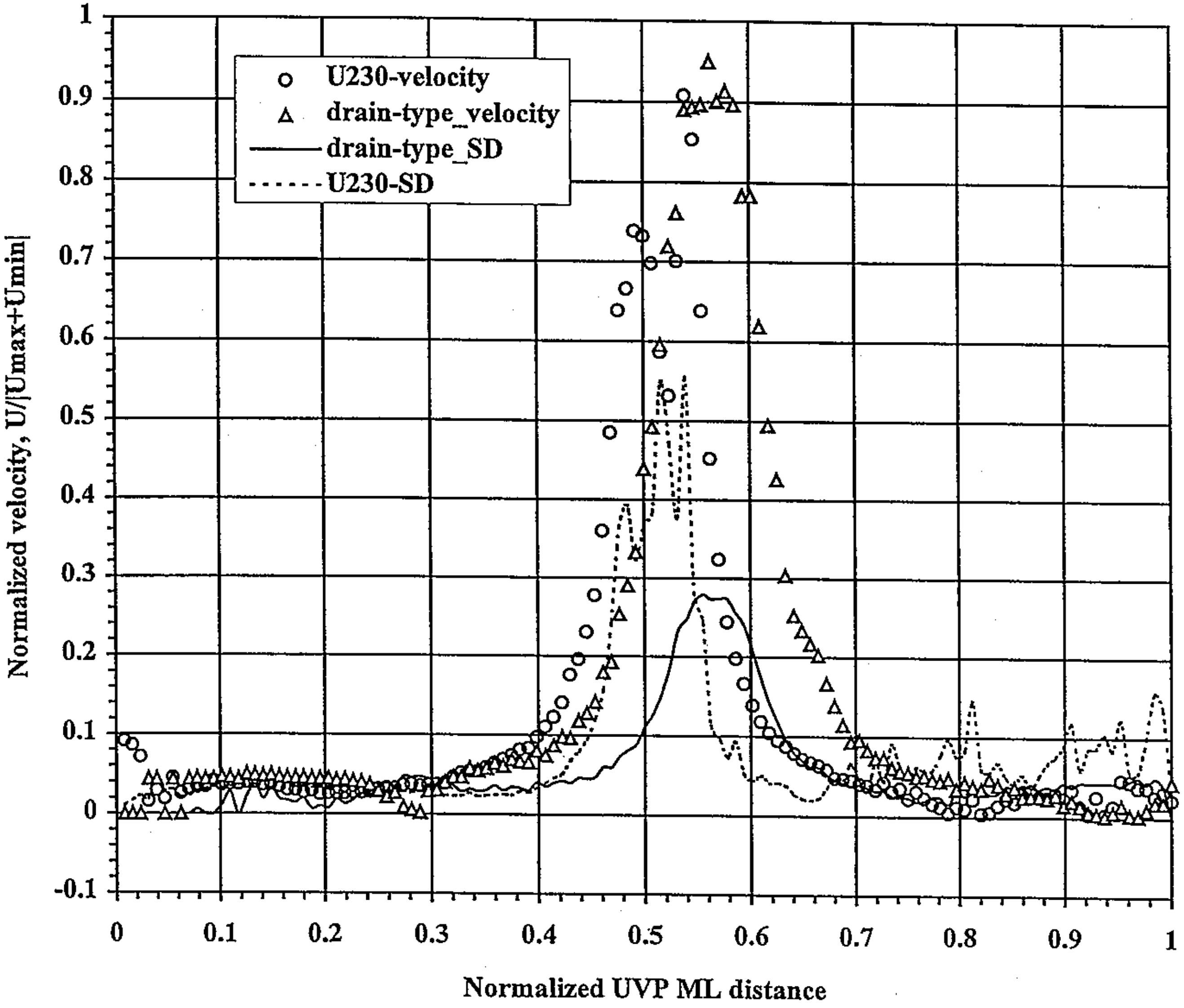

Figure 20. Velocity and SD profiles between stirring-induced and drain-type vortices.
Drain type is at Q=5 l/min; D=19.8 mm;Vr(z=0)

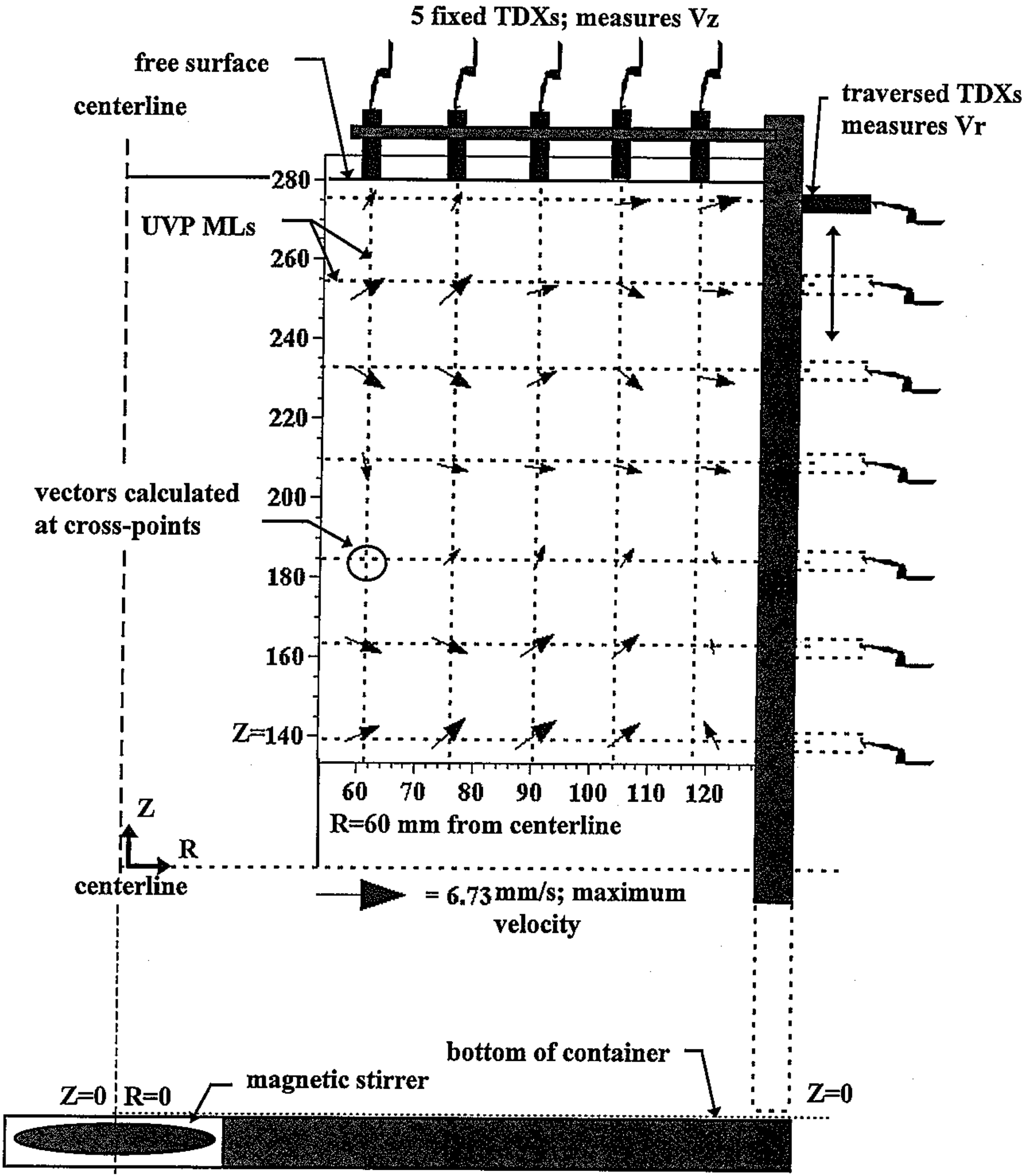

Figure 21. Approximate location of the measured 2D vector field with respect to the container and UVP TDX locations.

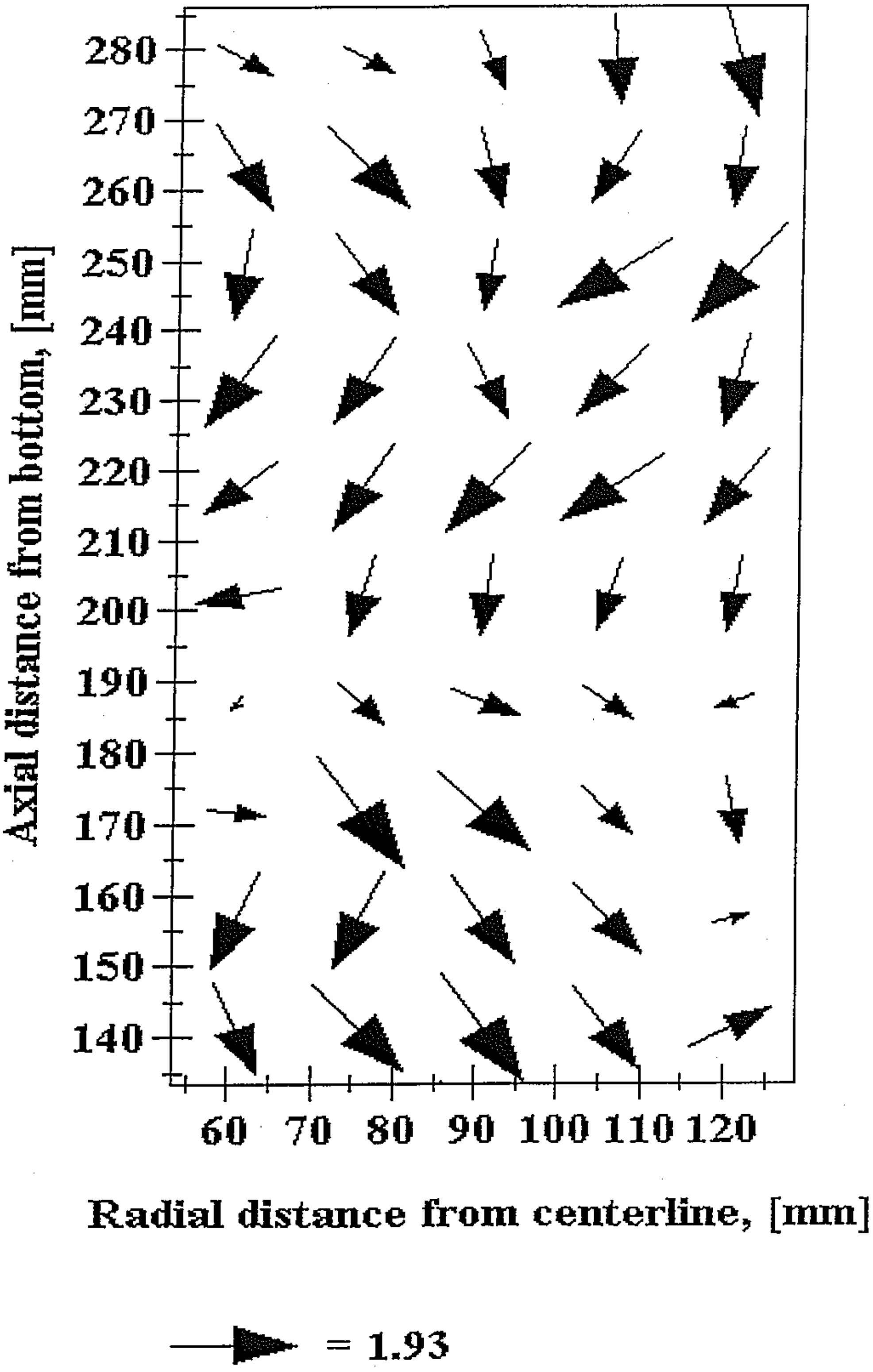

Figure 22. Measured 2D vector field at 230 rpm with five channel averaging.

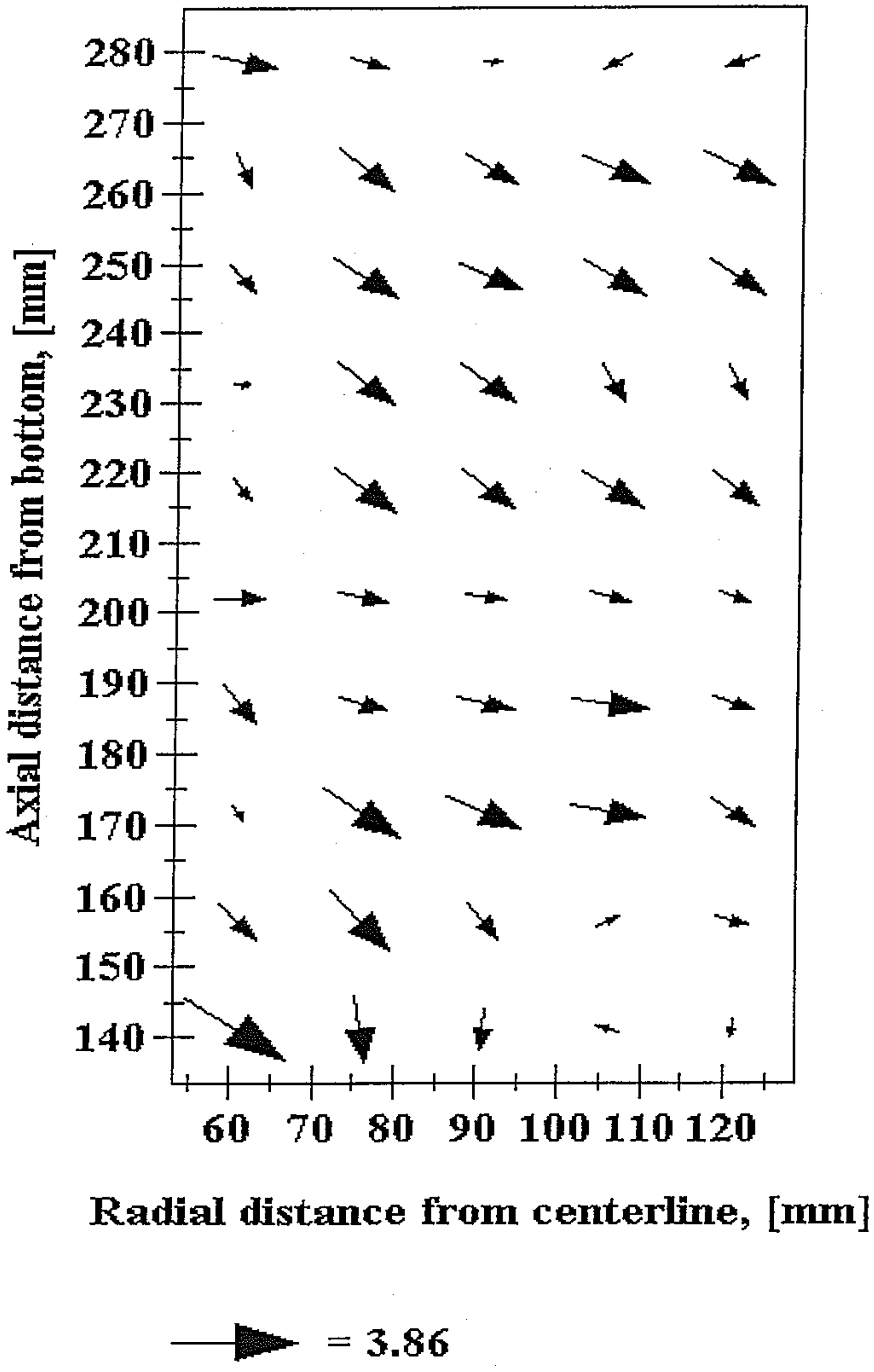

Figure 23. Measured 2D vector field at 410 rpm with five channel averaging.

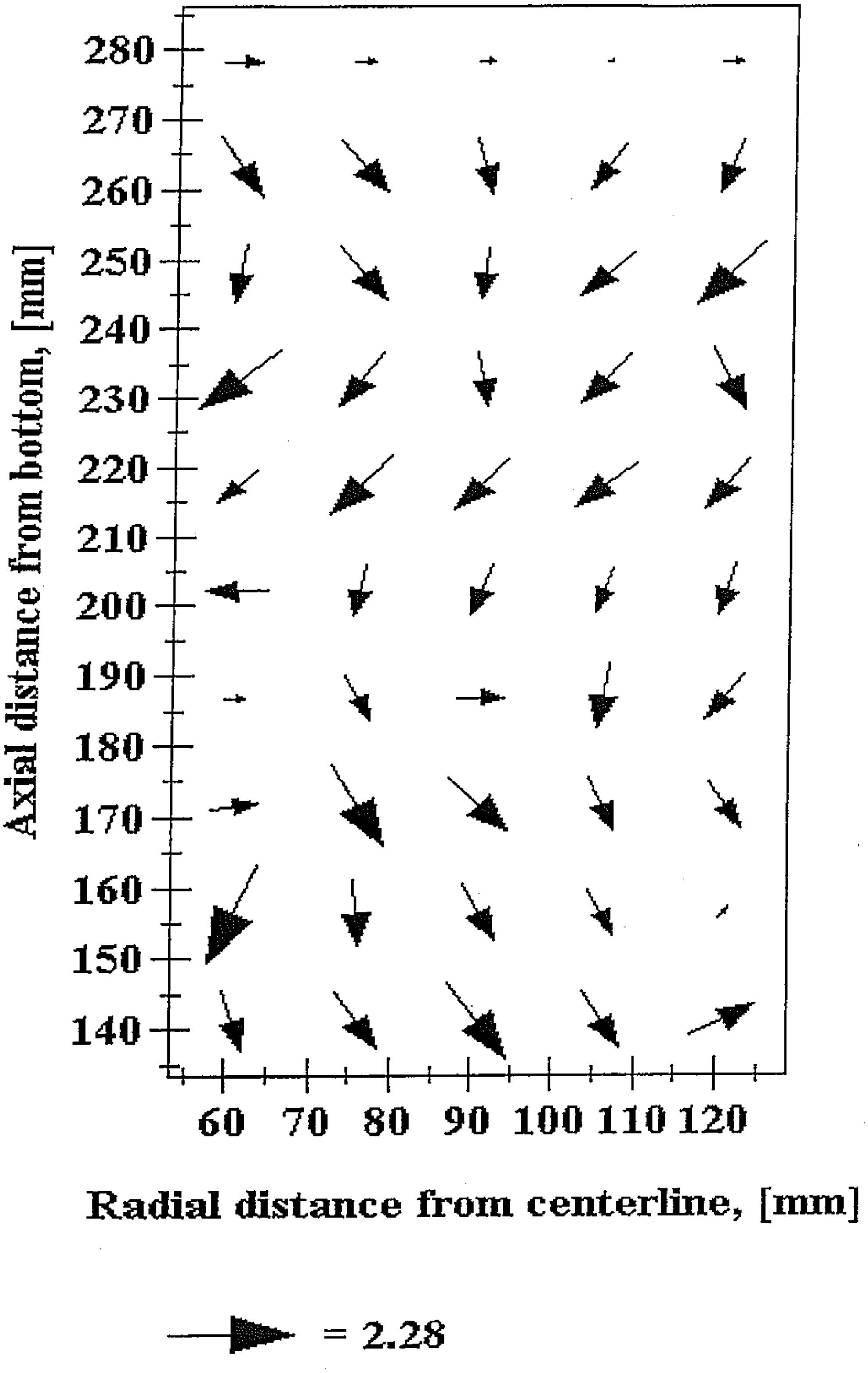

Figure 24. Measured 2D vector field at 230 rpm based on channel value closest to cross-points.

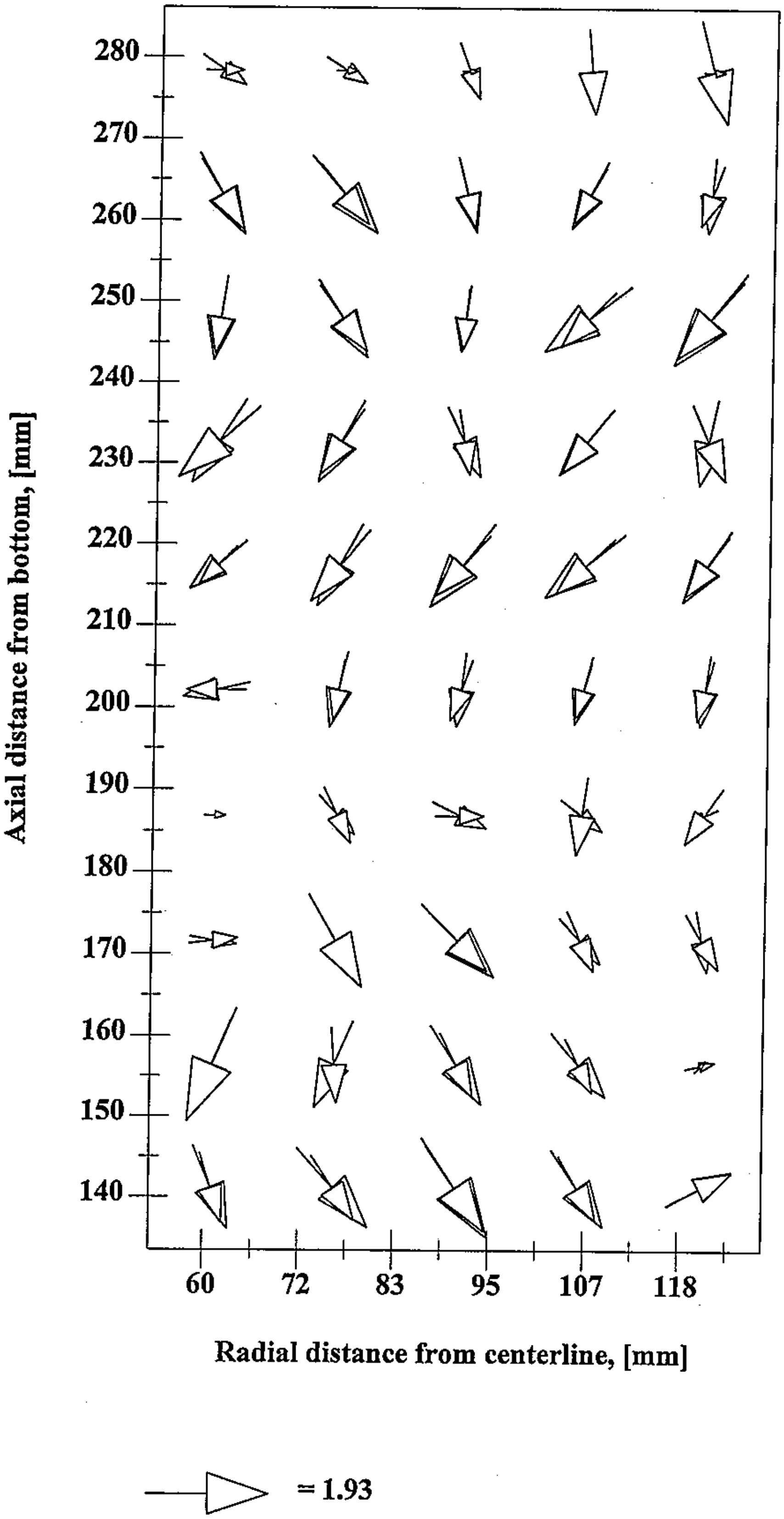

Figure 25. Direct comparison of vectors calculated as an average of 5 channels versus a channel closest to cross-points.

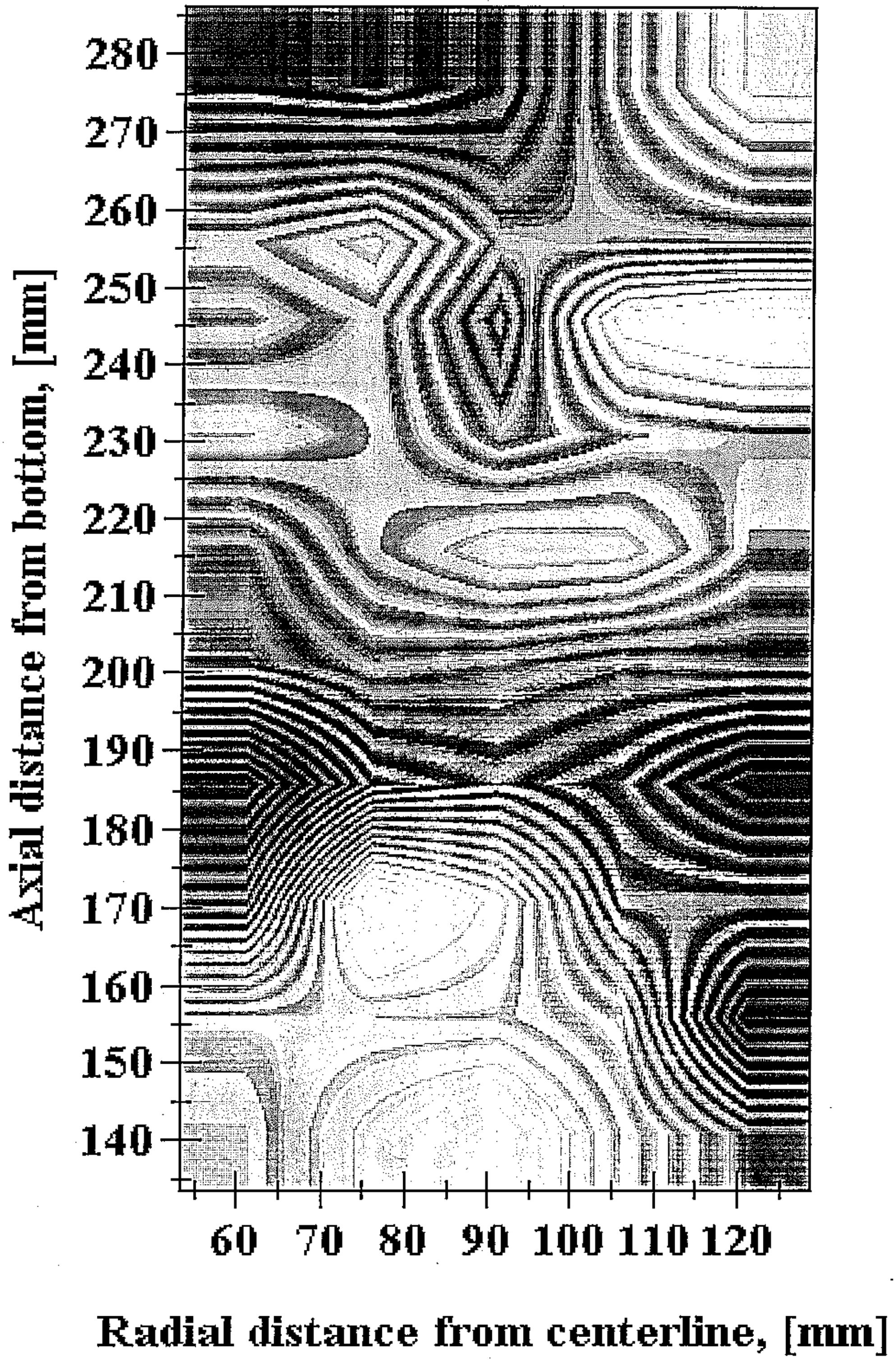

Figure 26. Grayscale, banded contour plot of the magnitude of the vector field at 230 rpm.

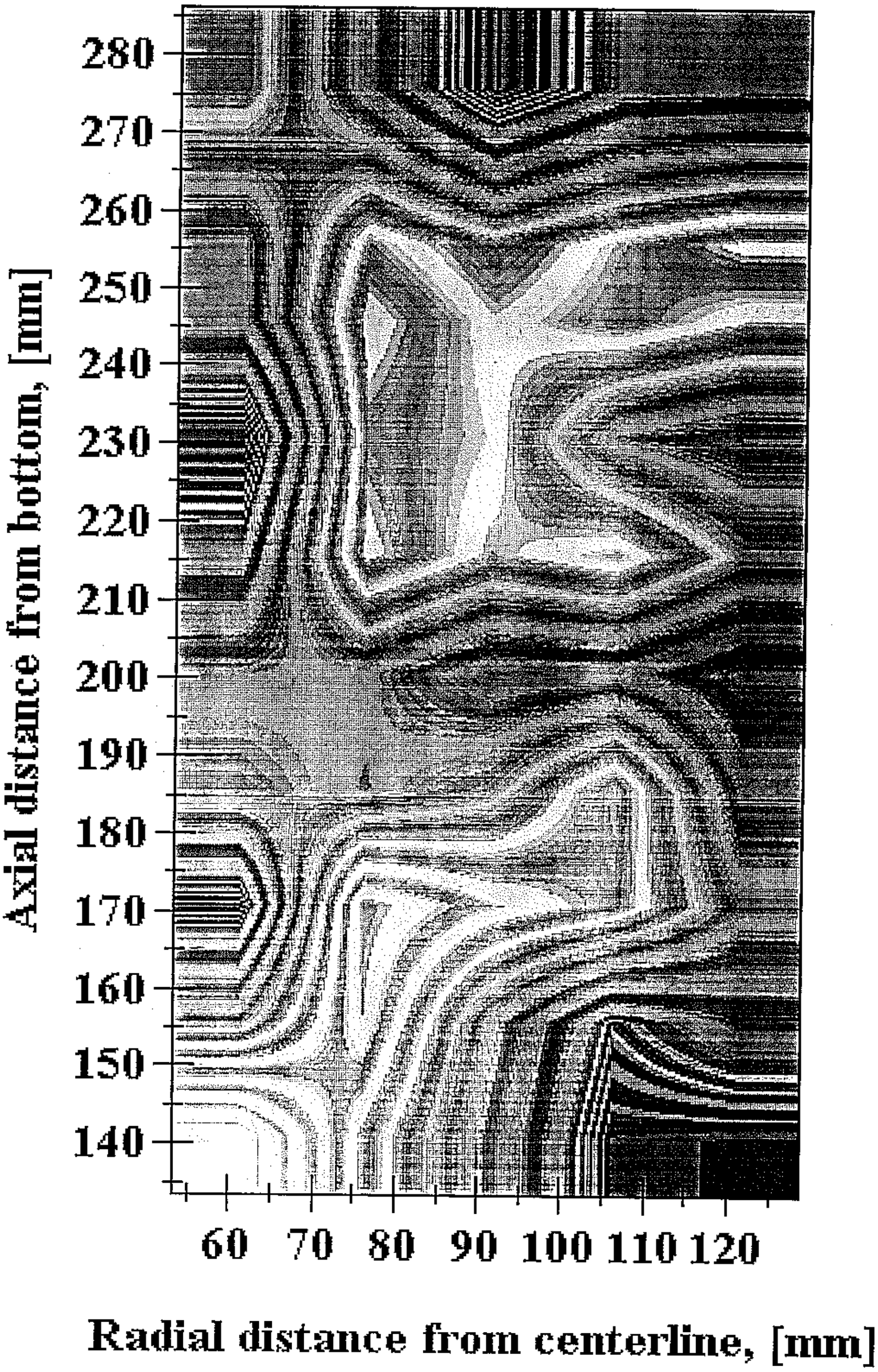

Figure 27. Grayscale, banded contour plot of the magnitude of the vector field at 410 rpm.

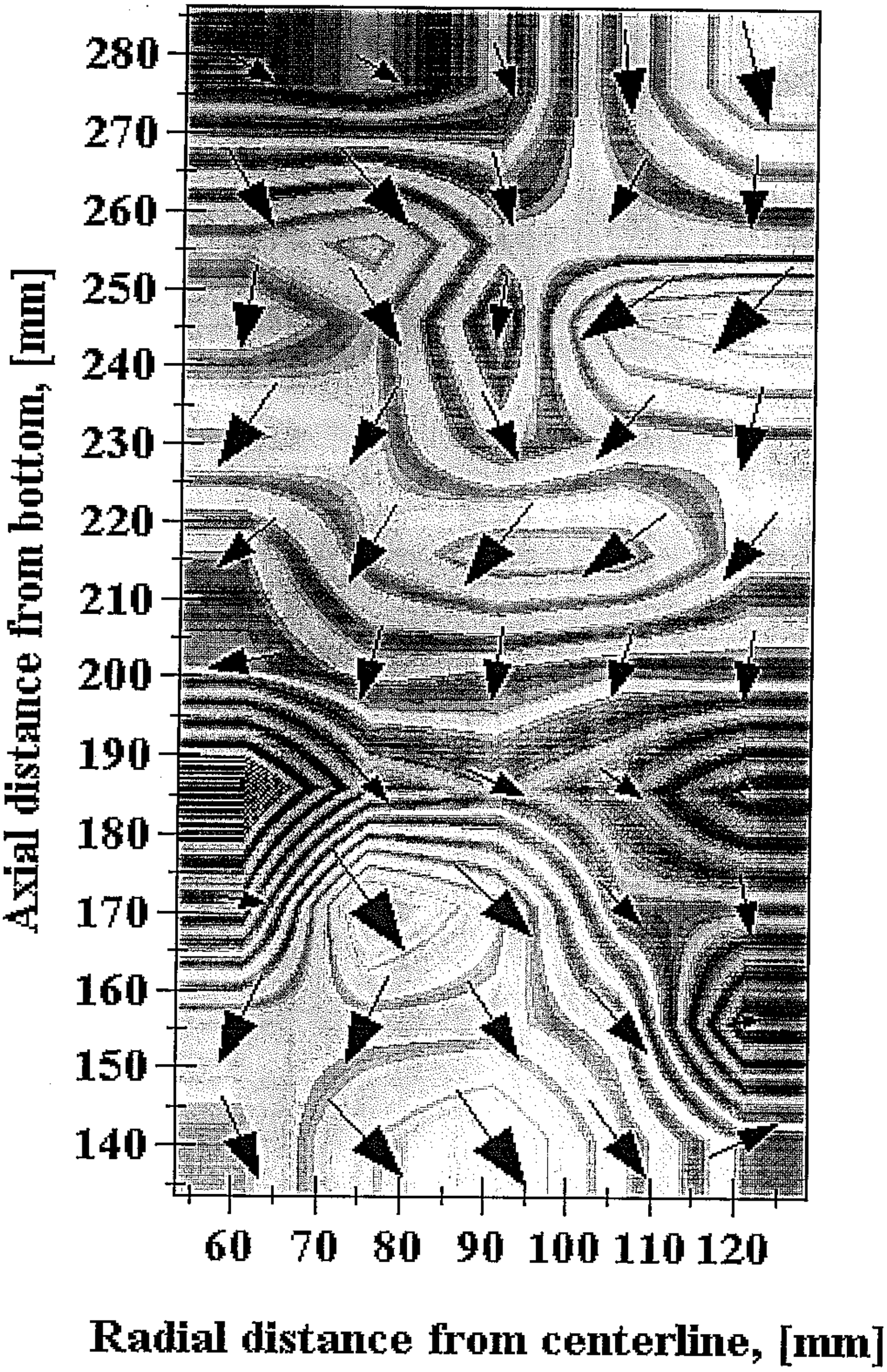

Figure 28. 2D vector field superimposed on top of a grayscale contour of the magnitude of the SD at 230 rpm.

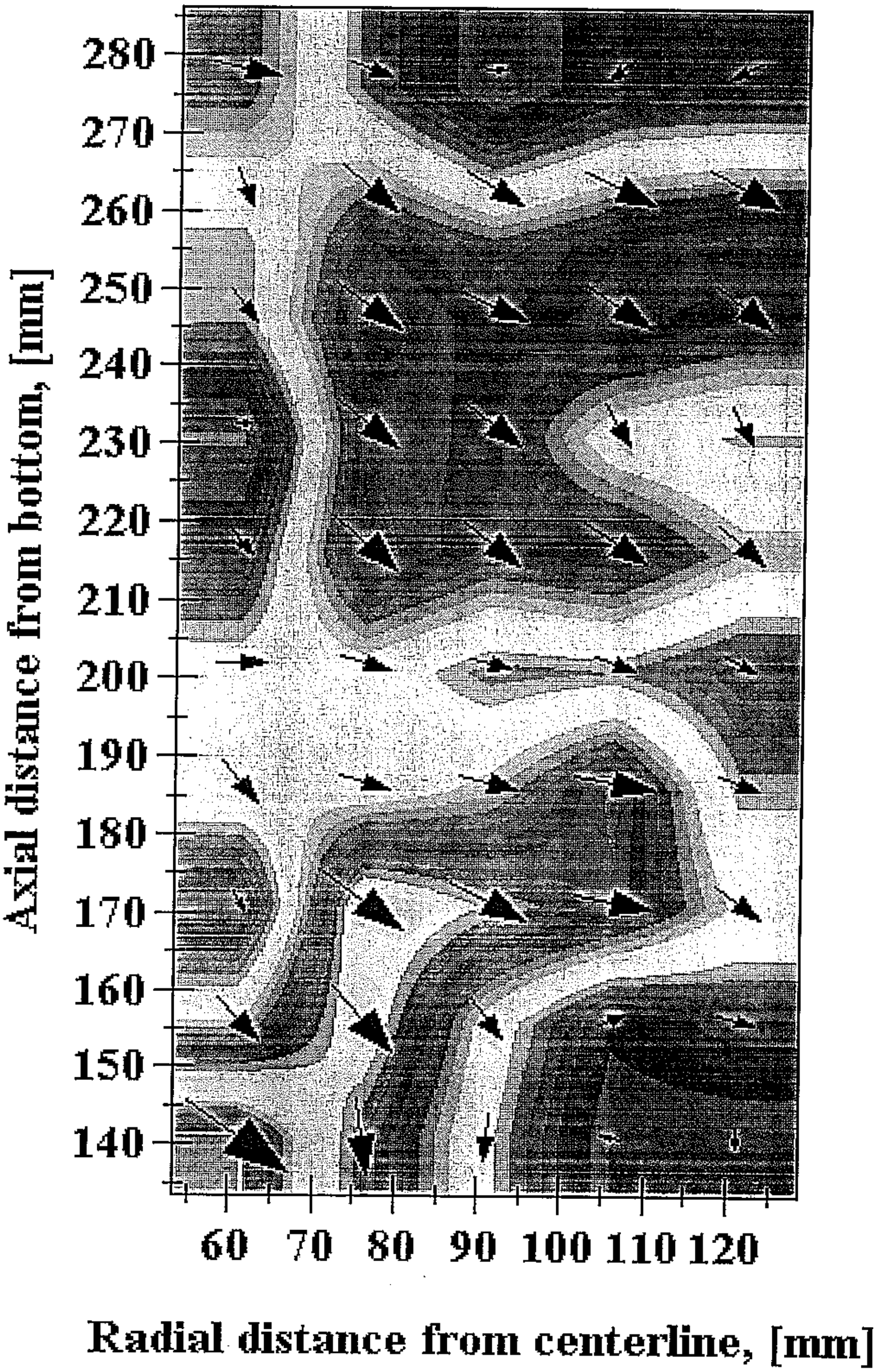

Figure 29. 2D vector field superimposed on top of a grayscale contour of the magnitude of the SD at 410 rpm.